Paraboloid model of Mercury's magnetosphere

I. I. Alexeev,[1] E. S. Belenkaya,[1] S. Yu. Bobrovnikov,[1] J. A. Slavin,[2] and M. Sarantos[2]

Received 5 May 2008; revised 1 September 2008; accepted 29 September 2008; published 17 December 2008.

[1] A new "Paraboloidal" model of Mercury's magnetospheric magnetic field based upon the earlier terrestrial model and using similar techniques is developed. The model describes the field of Mercury's dipole, which is considered to be offset from the planet's center; the magnetopause currents driven by the solar wind; and the tail current system including the cross-tail currents and their closure currents at the magnetopause. The effect of the interplanetary magnetic field (IMF) is modeled as a partial penetration of the IMF into the magnetosphere. The goals of the present work are (1) to develop an easily usable, yet robust model of Mercury's magnetospheric magnetic field and (2) to produce an improved "unified" determination of Mercury's magnetic dipole moment which fits the measurements taken during both Mariner 10's first and third flybys. This new model of Mercury's magnetosphere is described and used to determine a best Mercury magnetic dipole moment of 192 nT R_M^3, from the two Mariner 10 flybys, a value which is intermediate between the various estimates produced by previous models. The best fit to the Mariner 10 measurements gives the dipole offset 0.18 R_M above the equatorial plane. The new Paraboloidal model is used to predict the configuration of this miniature magnetosphere under average and extreme solar wind conditions.

Citation: Alexeev, I. I., E. S. Belenkaya, S. Yu. Bobrovnikov, J. A. Slavin, and M. Sarantos (2008), Paraboloid model of Mercury's magnetosphere, *J. Geophys. Res.*, *113*, A12210, doi:10.1029/2008JA013368.

1. Introduction

[2] Mercury is the nearest planet to the Sun having perihelion and aphelion distances of 0.309 and 0.469 AU, respectively. The magnetic dipole moment of Mercury determined from the first Mariner 10 fly-by was 5.1 ± 0.3·10^7 G·km^3 (351.5 ± 20.7 nT R_M^3) oriented at a solar ecliptic latitude of −80° ± 5° and a longitude of +285° ± 10° [*Ness et al.*, 1975], and had the same polarity as that of the Earth's with a tilt relative to the planetary rotation axis of ~10° [*Connerney and Ness*, 1988]. Recently the MESSENGER mission's first flyby has yielded new centered dipole determination of 230 to 290 nT R_M^3 with tilts of 5 to 12° to the rotation axis [*Anderson et al.*, 2008]. It has been hypothesized that the internal source of magnetic field is a fluid iron core with a radius of ~0.75 R_M [e.g., *Giampieri and Balogh*, 2001]. Mercury's rotational and orbital periods are 59 and 88 (Earth) days, respectively. The Mercury radius is R_M ~2439 km. The Hermean magnetosphere is very dynamic; a convection time scale has been estimated to be only ~1 min [*Siscoe and Christopher*, 1975; *Ogilvie et al.*, 1977]. Its size is about 5% of that of the Earth. The weak magnetic field results in ion gyro radii exceeding the distance to the subsolar point of the magnetopause even for relatively modest energies [*Wurz and Blomberg*, 2001; *Boardsen and Slavin*, 2007]. Within Mercury's magnetosphere, the plasma density is higher than at the Earth's plasma trough region by a factor comparable to the ratio of the external solar wind density at the orbits of these two planets [*Ogilvie et al.*, 1977]. Initial results from the first MESSENGER flyby indicate that Mercury's small magnetosphere is immersed in a tenuous, comet-like cloud of planetary ions with a very complex composition whose dominant ion is Na^+ [*Zurbuchen et al.*, 2008; *Slavin et al.*, 2008].

[3] Because of its close proximity to the Sun, the solar wind pressure and interplanetary magnetic field (IMF) intensity at Mercury's orbit are typically one order of magnitude higher than is the case at the Earth and more than two orders of magnitude greater than at Jupiter [see e.g., *Slavin and Holzer*, 1981]. The interaction of the solar wind and interplanetary magnetic field with predominantly dipolar planetary magnetic field has been studied and modeled extensively in the case of the Earth. Furthermore, it has also been shown that at Jupiter [*Belenkaya*, 2004; *Alexeev and Belenkaya*, 2005], and even at Saturn [*Belenkaya et al.*, 2006, 2007], the IMF exerts considerable control over the magnetospheric structure despite the strong energy input from planetary rotation and large satellite plasma sources and their distant locations from the Sun, where the values of solar wind pressure and IMF are greatly reduced.

[4] At Mercury perihelion typical solar wind conditions are: velocity ~400 km·s^{-1} and IMF ~27 nT, which produce an electric potential of ~40 kV applied to the day-side X-

[1]Institute of Nuclear Physics, Lomonosov Moscow State University, Leninskie Gory, Moscow, Russia.
[2]Heliophysics Science Division, NASA GSFC, Greenbelt, Maryland, USA.

Copyright 2008 by the American Geophysical Union.
0148-0227/08/2008JA013368

line with length of $\sim$1.5 R_M in a case of southward IMF (i.e., parallel to the Hermean magnetic dipole). For more extreme conditions, $\sim$ 500 km·s^{-1} and 90 nT, the potential drop applied to the magnetosphere could reach 165 kV [*Slavin*, 2004]. Furthermore, the efficiency of the dayside reconnection between the IMF and Mercury magnetic fields has been estimated to be 40%, or $\sim$ 3 to 4 times greater than at the Earth because of the high Alfven speed in the solar wind at 0.3 AU [*Slavin and Holzer*, 1979a]. Accordingly, solar wind-planet coupling is expected to be very important at Mercury.

[5] Although measurements are about to be released from the first of MESSENGER three flybys [*Solomon et al.*, 2001], the presently available observations of Mercury's magnetosphere are limited to three NASA's Mariner 10 encounters with the planet on 29 March 1974, 21 September 1974, and 16 March 1975 at a heliocentric distance of 0.46 AU. The relative orientation of Mercury with respect to the Sun was similar for all three encounters and Mercury was near aphelion. During the first encounter (MI) the closest approach to the surface was 723 km and the peak measured magnetic field was 98 nT [*Ness et al.*, 1974]. The second encounter (MII) with its closest approach of 50,000 km did not contact the magnetosphere. The third encounter (MIII) confirmed the global dipolar nature of the magnetic field and measured a maximum magnetic field of 400 nT at the closest approach altitude of 327 km over the north pole of the planet [*Ness et al.*, 1976].

[6] The Mariner 10 and MESSENGER observations strongly suggest that Mercury's magnetosphere has a structure similar to that of the Earth. For example, magnetospheric "polar caps" are defined to be regions of the "open" field lines that connect a planet to the high-latitude magnetosphere and the tail lobes before closing in the solar wind. The size of the polar caps at Mercury were estimated by *Ness* [1979] to be $\theta_{pc} = 17°–26°$, where this angle is the co-latitude of their equatorial boundary, a value similar to that at Earth. *Ogilvie et al.* [1977] found a linear spatial scaling relative to the Earth's magnetosphere of the order of 8. According to this scaling, the nightside reconnection x-line is expected to be at $\sim$−3 R_M at Mercury [*Slavin*, 2004]. The mean distances from the center of Mercury to the subsolar point of magnetopause and bow shock are $\sim$ 1.5 R_M and 1.9 R_M [*Ness et al.*, 1976; *Russell*, 1977; *Jackson and Beard*, 1977; *Slavin and Holzer*, 1979b], respectively. *Slavin and Holzer* [1979b] found that the subsolar distances extrapolated from the magnetopause and bow shock crossings, after scaling for upstream ram pressure effects, varied from 1.3 to 2.1 R_M with the largest values corresponding to IMF $B_z > 0$ and smaller to $B_z < 0$. However, it must be noted that induction currents generated in the planetary interior are expected to restrict motion of the magnetopause because of changing solar wind pressure [*Glassmeier et al.*, 2007]. The observed near-tail Hermean magnetosphere diameter is $\sim$5 R_M as compared with the typical near-tail diameter at Earth of $\sim$ 40 R_E [*Shue et al.*, 1998], where 1 R_E = 6380 km.

[7] Mercury has no significant atmosphere or ionosphere, just a tenuous exosphere [*Hunten et al.*, 1988; *Potter et al.*, 1999, and references therein]. The magnetospheric plasma is believed to come from two primary sources, the solar wind and the ionization of the neutral exosphere [*Cheng et al.*, 1987; *Ip*, 1986; *Killen et al.*, 2001]. Recent analysis of the Mariner 10 magnetic field data by *Boardsen and Slavin* [2007] has failed to find evidence of the ion cyclotron waves expected to be present if heavy ions from the exosphere are being incorporated into this small magnetosphere's thermal ion population. However, while their detailed properties are not yet known, the MESSENGER first flyby measurements do show that the magnetosphere is rich in planetary ions covering a wide range of species and charge states [*Zurbuchen et al.*, 2008]. *Russell* [1989] has interpreted ULF magnetic fluctuations measured by Mariner 10 close to the planet as being due to standing Alfven waves associated with closed field line resonances. *Slavin et al.* [1997] reported the presence of field-aligned currents in the magnetic field measurements taken during the first Mariner 10 flyby. However, the conducting path for their closure is not clear. *Blomberg* [1997] noted that if the necessary electrical conductivity is associated with the ionization of the neutral exosphere, it should exhibit large variations between the dayside and the nightside due to the large day-night asymmetries in atmospheric neutral populations observed to exist at Mercury [*Potter et al.*, 1999; *Killen et al.*, 2001]. In addition, *Grard* [1997] pointed out that the sunlit hemisphere of Mercury is covered by a photoelectron layer, which may play a role in the horizontal transport of charges and the coupling between the planet and its magnetosphere. However, the tenuous nature of Mercury's exosphere, as it is understood today, would support height integrated electrical conductance that is, at best, many orders of magnitude below those found in the ionosphere of the Earth, Jupiter, and Saturn [*Lammer and Bauer*, 1997].

[8] During MIII the interplanetary magnetic field was northward both before and after the encounter, and very smooth magnetic field variations were observed. *Siscoe et al.* [1975] explained the quiescent nature of the MIII magnetic field as being due to the unfavorable IMF $B_z > 0$ conditions for dayside reconnection and consequently by the low energy input to the magnetosphere at the time of this encounter. Indeed, the first MESSENGER encounter with Mercury on 14 January 2008 also took place under northward IMF conditions and observed relatively quite magnetic fields and no energetic particles very similar to what was observed during the third Mariner 10 fly-by [*Slavin et al.*, 2008]. Conversely, Siscoe et al. attributed the highly disturbed magnetic fields and hot plasmas observed during the outbound half of MI to terrestrial-type substorms to the IMF $B_z < 0$ observed upon exiting into the magnetosheath. The duration of a substorm at Mercury was found by Mariner 10 to be only a few minutes as compared to about 1 hr on Earth [*Siscoe et al.*, 1975]. However, it remains to be determined whether these disturbances are directly driven by dayside reconnection as suggested by *Luhmann et al.* [1998] or associated with the storage of energy in this planet's tail and sporadic, explosive release as seen in the Earth's magnetosphere [*Slavin et al.*, 2007].

[9] At present significant uncertainties exist regarding the contributions by magnetospheric current systems to the total magnetic field measured by Mariner 10. Progress on this important issue requires the development of more accurate magnetospheric current system models for Mercury [*Giampieri and Balogh*, 2001]. The present paper is

devoted to this problem. As has been shown by *Korth et al.* [2004] and *Anderson et al.* [2008], knowledge of the external magnetic field is also expected to be the primary limiting factor in reliable determination Mercury's magnetic moment from the new MESSENGER magnetic field measurements. It is for this reason that more flexible and accurate models of the Hermean magnetosphere are needed. Usually the magnetic field inside Mercury's magnetosphere is assumed to consist of an intrinsic dipole component and an external contribution due to a Earth-like magnetospheric current systems (e.g., Tsyganenko 96 model) with the ring current and field-aligned current contributions suppressed. Using such a magnetic field model of the different large-scale magnetospheric current systems generally allows a reasonable interpretation of the measured data [*Anderson et al.*, 2008]. However, the Paraboloidal model developed herein offers several advantages over scaled terrestrial models. In particular, the Paraboloidal model allows for magnetopause and tail current systems to be specified separately to better reflect conditions in this miniature magnetosphere as opposed to those found at the Earth. Furthermore, the Paraboloidal model also parameterizes separately the effects of the high reconnection efficiency and the IMF intensity and orientation and allows for the use of values similar to those found at Mercury appropriate to its location in the inner heliosphere. In contrast, the scaled Earth models cannot easily be modified to include any of these important factors. This point is very important for a number of reasons, including, for example, the dominance of the B_x component of the IMF at Mercury's orbit that may be critical to understanding the structure and some dynamical aspects of this magnetosphere as was emphasized by *Luhmann et al.* [1998] and *Sarantos et al.* [2007].

2. Existing Models of Mercury's Magnetosphere

2.1. Magnetospheric Models With Fixed Magnetopause and MHD Models

[10] *Sarantos et al.* [2001] emphasized that as a consequence of the location of Mercury, the B_x component of the IMF is dominant. The Parker spiral angle that the IMF makes with the radial direction at Mercury is $\sim 20°$ for typical solar wind conditions. They used a modified model of *Toffoletto and Hill* [1993] (hereinafter TH93) to study how changes in the IMF affect the access of solar wind ions to the surface and, indirectly, the supply of neutrals to the exosphere sputtered from Mercury's surface. TH93 is an analytical model, in which the shape of the magnetopause consists of a semi-infinity cylinder on the nightside attached to hemisphere on the dayside. For a closed model, the normal component of the magnetic field at the magnetopause is zero everywhere. For an open magnetosphere, a so-called "inter-connection" magnetic field was added as a perturbation to the closed magnetic field model. The normal magnetic field component to the magnetopause is a free parameter. Following the suggestion of *Slavin and Holzer* [1979b] regarding the high efficiency for reconnection expected at Mercury, *Sarantos et al.* [2001] normalized and adjusted their interconnection field so that the penetration fraction of the IMF at Mercury is 40% for southward IMF. The tilt of Mercury's dipole was assumed to be zero. Using a variety of possible magnetospheric configurations, *Sarantos et al.* [2001] showed that the location and extent of the polar cap area is regulated primarily by changes in the IMF direction and magnitude.

[11] In the model developed here we assume the shape of magnetopause to be a paraboloid of revolution in contrast to the hemisphere plus semi-infinite cylinder of TH93. We plan to limit applications of our model mainly to dayside and near tail magnetosphere. For the forward magnetosphere ($X > -2 - -3\ R_M$) the paraboloid of revolution approximates the Hermean magnetopause very well. In the region under consideration for intrinsic magnetic field modeling and charged particle motion this approximation is better than that one presented by *Sarantos et al.* [2001]. Two additional factors also support this modeling approach: (1) The parabolic coordinate system is one of three orthogonal coordinate systems (along with spherical and cylindrical systems) for which a Schrödinger's type of equation (i.e., magnetic field diffusion equation) has a solution which can be presented as a product of the single variable functions. This fact gives us a possibility to have a solution of the problem as an expansion of the well-known special functions and to easily find any asymptotic behavior of the solution. (2) In the cusp region we have a focus of the magnetopause currents system with the current density becoming zero at the cusp and small around the cusp. The displacement of these currents will have insignificant influence on the magnetopause current field at any point inside the magnetosphere excluding the region near the cusp.

[12] Global MHD [*Kabin et al.*, 2000; *Ip and Kopp*, 2002] and hybrid [*Kallio and Janhunen*, 2003a, 2003b; *Travnicek et al.*, 2007] simulations of the solar wind interaction with Mercury have produced qualitatively similar results, especially with respect to the strong effects of IMF B_z and B_x on the magnetic topology of the dayside magnetosphere. For example, each of these studies calculated the size of the Hermean polar cap. *Kabin et al.* [2000] estimate the latitudes of the open/closed field line boundary as $\approx 50°$; *Kallio and Janhunen* [2003a, 2003b] placed the polar cap boundary between 30° (midnight) and 60° (noon); *Ip and Kopp* [2002] found that the IMF orientation is very effective in controlling the size of the polar cap with a mean location of about 60°. Both the MHD and hybrid numerical simulations of the solar wind interaction with Mercury support the terrestrial-type magnetosphere interpretation of the Mariner 10 of *Ogilvie et al.* [1977] and MESSENGER [*Slavin et al.*, 2008] observations and the short convective time scale for substorms and other effects of reconnection suggested by *Siscoe et al.* [1975].

2.2. Estimates of Mercury's Magnetospheric Currents and Dipole Moment From Modeling Mariner 10 Magnetic Field Measurements

[13] Different estimations of the magnetic moment of Mercury have been obtained from observations during the MI and MIII flybys [*Connerney and Ness*, 1988; *Anderson et al.*, 2007]. *Ness et al.* [1974] found a dipole moment of 227 nT R_M^3, conducting a least-squared fit of the MI data to an offset titled dipole with a tilt angle of 10° relative to the planetary rotation axis. *Ness et al.* [1975] obtained from the same data set a moment of 349 nT R_M^3 utilized a centered dipole and an external contribution to the measured mag-

netic field. *Ness et al.* [1976] determined a dipole moment of 342 nT R_M^3 from the MIII observations. *Jackson and Beard* [1977] and *Whang* [1977] included quadrupole and quadrupole - octupole terms for the internal magnetic field obtained with a resultant reduction in the dipole moment to $\sim$ 170 nT R_M^3. Ultimately, the cause for the large range of dipole moment estimates, i.e., $\sim$ 150 to 350 nT R_M^3, derived from the Mariner 10 measurements is the small volume sampled by this mission and the highly variable contributions of the magnetospheric current systems to the total measured field [*Slavin and Holzer*, 1979a; *Connerney and Ness*, 1988]. Furthermore, these variable contributions from the magnetospheric currents are strongly controlled by the solar wind and the IMF, and the Mariner 10 encounters took place under very different upstream conditions. For these reasons it is not surprising that the "static" scaled Earth models that have been used up to this point have produced very different planetary magnetic dipole determinations for each Mariner 10 encounter and, in the case of MI, even different portions of the same encounter. Below we consider these previously elaborated scaled Earth-like magnetospheric models in more detail.

[14] *Lukyanov et al.* [2001] developed a model of Mercury's magnetosphere by scaling the Tsyganenko terrestrial model [*Tsyganenko*, 1989] to Mercury. To scale the Earth magnetospheric magnetic field at some point $\mathbf{R}'$ to the Hermean magnetospheric magnetic field at some point $\mathbf{R}$, Lukyanov et al. have used the formula:

$$\mathbf{B}_{Merc}(\mathbf{R}) = k_m \mathbf{B}_{Earth}(\mathbf{R}'), \text{ where } \mathbf{R}' = k_s \frac{R_E}{R_M}\mathbf{R}, \text{ and } k_m = k_s^3 \frac{\mu_M R_E^3}{\mu_E R_M^3} \quad (1)$$

Here R_M = 2439 km and R_E = 6380 km are the Mercury's and Earth's radii, μ_M and μ_E are the respective magnetic moments, k_m is a magnetic field scaling factor, and k_s is a spatial-scale factor for the Mercury's magnetosphere. *Lukyanov et al.* [2001] mentioned that the ratio of the Mercury and Earth dipole magnetic moments is 10^{-3}, however, it should be noted that using for Mercury μ_M = 300 $nT \cdot R_M^3$ from this paper, one will obtain a value about two times smaller: $\frac{\mu_M}{\mu_E} = \frac{300 nT \cdot R_M^3}{30000 nT \cdot R_E^3} = 5.54 \cdot 10^{-4}$. Since the *Tsyganenko* [1989] model of has no well-defined magnetopause, *Lukyanov et al.* [2001] chose to represent its shape in a form $r = l/(1 + \varepsilon \cos \theta)$, where r is the radial distance to the magnetopause, l is the radial distance to the magnetopause in the terminator plane, ε is the eccentricity of the conic surface, and θ is the Sun-planet-satellite angle [see *Russell*, 1977; *Slavin and Holzer*, 1981]. For Mercury, *Russell* [1977] found $l = 2.24 \pm 0.4$ R_M and $\varepsilon = 0.6 \pm 0.1$ and the corresponding subsolar magnetopause distance, R_{sM}, is 1.4 R_M. However, the magnetopause surface chosen by *Lukyanov et al.* [2001] served only as a boundary of the simulation box for particle orbit tracing, so it was not a factor in the representation of the magnetospheric magnetic field.

[15] *Engle* [1997] modeled the Hermean magnetosphere-magnetotail system using the MI and MIII flyby data of the Mariner 10 mission. When the magnetic field data from the first half of the MI flyby and all of the MIII flyby were incorporated into the scaled version of the model of *Beard* [1979], a rms deviation of 9.3 nT for each component of the magnetic field vector was obtained [*Bergan and Engle*, 1981]. The tail-field representation of Beard is appended to the near-planet region. Engle presents results of a study that includes an adaptation of that model of Beard, but also adopts the assumption that the incident solar wind pressure and/or direction of the solar wind was different for the two Mariner 10 flybys. The subsolar magnetopause distances assumed in these models were 1.08 R_M and 1.31 R_M, respectively, for MI and MIII. A non-linear least-squares fit was produced by varying each parameter in turn to minimize the deviation of the model magnetic field from the observed data. In this Mercury magnetosphere adaptation, Engle separately scaled the "near-planet" region and the magnetotail region representation functions. This allowed a reduction in the rms deviation between the model and the Mariner 10 observations of 7.1 nT. Furthermore, the Mercury dipole was linearly displaced from the planet center. The dipole moment estimates produced by Engle varied between 154 nT R_M^3 (MI) and 182 nT R_M^3 (MIII).

[16] *Luhmann et al.* [1998] used a scaled *Tsyganenko* [1995] terrestrial magnetospheric model that included the effects of IMF B_y and B_z and an assumed IMF variation during the disturbed MI outbound pass segment. They noted that changes in IMF occurring on the time scale $\sim$1 min or longer may affect the near-Mercury magnetosphere in a "quasi-steady" manner from the IMF control point of view. It was proposed that the IMF strength was constant during the MI flyby and only its orientation changed. *Luhmann et al.* [1998] calculated magnetospheric magnetic field for zero IMF, and the difference between the modeled and measured fields was attributed to the IMF B_y and B_z influence using simple superposition.

[17] Recently, *Kabin et al.* [2008] used an MHD model of the solar wind-Hermean magnetosphere interaction to forecast the magnetospheric field along MESSENGER orbits. They estimated the dipole field as 350 nT R_M^3 and a symmetric quadrupole aligned with the Z axis with quadrupole moment 45 nT R_M^4.

3. Paraboloidal Model of Mercury's Magnetic Field

3.1. Background

[18] We now construct a new magnetic field model for Mercury using the well known "Paraboloidal" model of the Earth's magnetosphere. A summary of this model can be found in the work of *Alexeev* [1986]. The name of this model is derived from its key simplifying assumption that the magnetopause be represented as a paraboloid of revolution about the planet-Sun line. The field due to magnetopause currents and tail current system is obtained using a method pioneered by *Alexeev* [1978] wherein the magnetic fields of the various magnetospheric sources are confined inside the magnetopause by adding appropriate shielding fields. Paraboloidal models have also been developed and successfully tested against magnetic field measurements taken at Jupiter and Saturn [*Belenkaya*, 2004; *Belenkaya et al.*, 2005, 2006, 2007; *Alexeev and Belenkaya*, 2005; *Alexeev et al.*, 2006]. As mentioned earlier, this model is very robust in that the amount of open magnetic flux in the polar cap and the effects of interplanetary magnetic field intensity and direction can be specified in a manner appropriate to each planetary magnetosphere.

[19] In the analysis to follow Mercury-centered solar orbital (MSO) coordinates are employed. In this system X_{MSO} is directed toward the Sun, Y_{MSO} is perpendicular to X_{MSO} in Mercury's orbital plane and positive toward dusk, and Z_{MSO} completes this right-handed orthogonal system. Mercury's magnetic moment M_M lies in the X-Z plane. The main contributors to the magnetic field in the miniature Hermean magnetosphere according to this model are: (1) the intrinsic magnetic (dipole) field of the planet and the shielding magnetopause current which confines the dipole field inside the magnetopause, (2) the dawn-dusk cross-tail currents and their closure currents on the magnetopause, and (3) the IMF which partially penetrates into the magnetosphere as a result of "reconnection" with the planetary magnetic field.

[20] The following parameters define Mercury's magnetospheric magnetic field in the Paraboloidal model: (1) R_{sM} is the distance from Mercury's center to the subsolar point on the magnetopause; (2) R_2 is the distance from the planet's center to the inner edge of the magnetospheric tail current sheet; (3) B_{M0} is the magnetic field at the Mercury's equator due to the dipole field only; (4) the magnitude of the magnetic field at the inner edge of the tail current sheet due only to that current sheet is B_t/α_0, where $\alpha_0 = (1+2R_2/R_{sM})^{1/2}$; (5) Ψ is the tilt angle between the magnetic dipole direction and the Z_{MSO} direction, although it is assumed here, for simplicity in this first application of our model, that the magnetic dipole of Mercury has no tilt; (6) z_0 is the displacement of the tail current sheet relative the magnetic equatorial plane; and (7) the portion, $\boldsymbol{b}$, of the IMF, $\boldsymbol{B}$, penetrating into magnetosphere, given as $\boldsymbol{b} = k_{IMF}\,\boldsymbol{B}$ where k_{IMF} is the coefficient of IMF penetration into the Hermean magnetosphere. *Tsyganenko* [2002] found the best correspondence between his model of the near-Earth magnetosphere and observational data for the coefficient of IMF penetration into the Earth's magnetosphere of between 0.15 and 0.8. For comparison, *Slavin and Holzer* [1979a] estimated the efficiency of the dayside reconnection at Mercury to be 40% because of the low solar wind Alfven Mach numbers typical of the inner heliosphere.

[21] The magnetopause is approximated as a paraboloid of revolution

$$X/R_{sM} = 1 - (Y^2 + Z^2)/2R_{sM}^2. \tag{2}$$

The appropriateness of such a shape for the forward magnetopause is supported by the boundary fitting of *Russell* [1977]. He found a near paraboloidal shape, i.e., eccentricity 0.8 versus 1.0 for a true parabola, for Mercury's magnetopause using the Mariner 10 observations. With these assumptions it will be demonstrated that the Paraboloidal model formulation of *Alexeev* [1986] can be used to calculate the magnetic configuration of Mercury's magnetosphere.

3.2. Screened Dipole Magnetic Field

[22] A first solution of the problem of the screened planetary dipole field within model magnetopause approximated by a paraboloid of revolution was obtained by *Alexeev and Shabansky* [1972]. They presented a solution of the Neumann problem by direct integration of the normal to magnetopause dipole magnetic field. Later *Stern* [1985] repeated this solution, but added a representation of the magnetopause current fields, as a sum of Bessel harmonics. The next step was taken by *Greene and Miller* [1994]. They conceived a simpler way to construct a solution and provided integral representations of the screened planetary dipole field within a paraboloid magnetopause with arbitrary magnetopause flaring angle. This solution created the possibility of describing the magnetopause with arbitrary ratio of dawn-dusk magnetopause size to the subsolar magnetopause distance. Below we follow the solution of *Greene and Miller* [1994].

[23] A detailed description of the screened planetary dipole field within the model magnetopause has been presented, for example, by *Belenkaya et al.* [2005] for the Jovian magnetosphere. The same method can be used to construct the topology of the Hermean magnetosphere. The parabolic coordinates (α, β, φ) with respect to the solar-magnetospheric Cartesian coordinates (X, Y, Z) can be defined by the following relations:

$$X = \frac{R_{sM}}{2}\left(\beta^2 - \alpha^2 + 1\right) \tag{3a}$$

$$Y = R_{sM}\alpha\beta\sin\varphi \tag{3b}$$

$$Z = R_{sM}\alpha\beta\cos\varphi, \tag{3c}$$

where X points toward the Sun and the X-Z plane contains the planetary dipole, φ is an azimuthal angle around the X axis, and R_{sM} is a scale length determining magnetopause size. The surfaces $\alpha = const$ and $\beta = const$ form paraboloids of revolution about the X axis with opposite curvature to each other (see for details *Belenkaya et al.* [2005]). To transform a vector $\boldsymbol{B}$ from parabolic to solar-magnetospheric Cartesian coordinates (X, Y, Z) we can use a matrix:

$$B_x = -\frac{\alpha}{\sqrt{\alpha^2+\beta^2}}B_\alpha + \frac{\beta}{\sqrt{\alpha^2+\beta^2}}B_\beta$$

$$B_y = \frac{\beta\sin\varphi}{\sqrt{\alpha^2+\beta^2}}B_\alpha + \frac{\alpha\sin\varphi}{\sqrt{\alpha^2+\beta^2}}B_\beta + \cos\varphi B_\varphi$$

$$B_z = \frac{\beta\cos\varphi}{\sqrt{\alpha^2+\beta^2}}B_\alpha + \frac{\alpha\cos\varphi}{\sqrt{\alpha^2+\beta^2}}B_\beta - \sin\varphi B_\varphi$$

Since the combined field (dipole plus magnetopause current field) is curl-free within the magnetosphere, it can be described by a scalar potential U ($\boldsymbol{B} = -\nabla U$):

$$U_{d+sd} = U_d^{\perp} + U_{sd}^{\perp}, \tag{4}$$

where $U_d^{\perp} = \mu_M\frac{z}{r^3}$ is the scalar potential of the Mercury dipole and $U_{sd}^{\perp}$ is the corresponding scalar potential of the screening field produced by the magnetopause currents. Here the planetocentric distance, r, is $r = \sqrt{x^2+y^2+z^2} = \frac{R_{sM}}{2}\sqrt{\left(\alpha^2+\beta^2+1\right)^2 - 4\alpha^2}$, and $4\pi\mu_M/\mu_o$ is the Hermean dipole moment (μ_M is equal to 192 $nT \cdot R_M^3$, as it will be shown below in the present paper by fitting Mariner 10 data). For simplicity, we propose that dipole is directed perpendicular to the planet-Sun line.

Table 1. Zeros of the Derivative of the Bessel Functions λ_{nk} ($J_n'(\lambda_{nk}) = 0$)

n/k	1	2	3	4	5
1	1.841183900	5.3314427000	8.5363163000	11.706005000	14.863588700
3	4.2011889412	8.0152365984	11.345924311	14.585848286	17.788747866
5	6.4156163752	10.519860874	13.987188630	17.312842488	20.575514521
7	8.5778364889	12.932386237	16.529365884	19.941853366	23.268052926
9	10.711433969	15.286737667	19.004593538	22.501398726	25.891277276
11	12.826491226	17.600266557	21.430854238	25.008518704	28.460857279

[24] To calculate the field of the screened planetary dipole we employ the following integral transform [e.g., *Gradshteyn and Ryzhik*, 1971]

$$\int_0^\infty \lambda^2 J_1(\lambda\alpha)K_1(\lambda\beta)J_1(\lambda)d\lambda = \frac{4\alpha\beta}{\left[\left(\alpha^2+\beta^2+1\right)^2-4\alpha^2\right]^{3/2}} = \frac{zR_{sM}^2}{2\cos\varphi r^3} = \frac{U_d^\perp}{M_M\cos\varphi}, \quad (5)$$

where J_1 are Bessel functions of the first kind, K_1 are modified Bessel functions that have a singularity at the origin, and the constant M_M is determined by dipole moment and subsolar magnetopause distance as $M_M = 2\mu_M/R_{sM}^2$. We have used here and below the Bessel functions definitions from *Abramowitz and Stegun* [1972]. For arbitrary function $f(\lambda)$ the integral $\int_0^\infty \lambda J_1(\lambda\alpha)K_1(\lambda\beta)f(\lambda)d\lambda$ multiplied by $\cos\varphi$ is a solution of the Laplace equation in the parabolic coordinates.

[25] Using the transform (5) we can write two terms of the potential U_{d+sd} (equation (4)) as

$$U_d^\perp + U_{sd}^\perp = M_M\cos\varphi\int_0^\infty \lambda^2 J_1(\lambda)J_1(\lambda\alpha) \cdot \left(K_1(\lambda\beta) - I_1(\lambda\beta)\frac{K_1'(\lambda)}{I_1'(\lambda)}\right)d\lambda, \quad (6)$$

where the primes indicate derivatives with respect to the argument, while the I_n are the modified Bessel functions that have no singularity inside the magnetosphere. After calculation of the derivative of β with respect to function inside the brackets, and taking $\beta = 1$ (magnetopause), we can see that first and second terms inside the brackets cancel each other: $K_1'(\lambda) = I_1'(\lambda)\frac{K_1'(\lambda)}{I_1'(\lambda)}$. The potential for the combined field, which is determined by equations (4) and (6), confines the magnetic field inside the magnetosphere ($B_\beta = 0$ at the magnetopause). This can be verified from the following expressions for the magnetic field components in parabolic coordinates

$$B_\alpha = -\frac{1}{R_{sM}\sqrt{\alpha^2+\beta^2}}\frac{\partial U}{\partial\alpha} \quad (7a)$$

$$B_\beta = -\frac{1}{R_{sM}\sqrt{\alpha^2+\beta^2}}\frac{\partial U}{\partial\beta} \quad (7b)$$

and

$$B_\varphi = -\frac{1}{R_{sM}\alpha\beta}\frac{\partial U}{\partial\varphi}. \quad (7c)$$

3.3. Field of the Tail Current System

[26] The model for the tail field adopted here is a modification of that previously proposed for the terrestrial [*Alexeev et al.*, 2003] and Jovian [*Belenkaya et al.*, 2005] magnetospheres. The tail field can be presented as a sum of two terms $\boldsymbol{B} = \boldsymbol{B}_1 + \boldsymbol{B}_2$. The most significant of them is the second term $\boldsymbol{B}_2$, which is associated with the current flowing in the centre plane of the tail, $\boldsymbol{j} = \text{curl}\,\boldsymbol{B}_2/\mu_o$, which is closed over the tail magnetopause. The first term, $\boldsymbol{B}_1$, is then a curl-free field that describes the closure of the tail field lines inside the magnetopause in the inner part of the system.

[27] In parabolic coordinates we define $\boldsymbol{B}_2 = (B_{2\alpha}, 0, 0)$, where (see *Belenkaya et al.* [2005] for details)

$$B_{2\alpha} = B_t\begin{cases} 0 & \text{for} \quad \alpha < \alpha_o, \\ \dfrac{f(\beta,\varphi)}{\alpha\sqrt{\alpha^2+\beta^2}} & \text{for} \quad \alpha > \alpha_o. \end{cases} \quad (8)$$

This field is divergence-free everywhere except on the surface $\alpha = \alpha_o$, inside of which (i.e., for $\alpha < \alpha_o$) the field and current both drop to zero. On the X-axis, the inner edge of the tail current sheet thus lies at a down-tail distance from the planet given by $R_2 = R_{sM}(\alpha_o^2 - 1)/2$. The divergence of $\boldsymbol{B}_2$ on $\alpha = \alpha_o$ is then accommodated by the curl-free field $\boldsymbol{B}_1$, as will be described below.

[28] The function $f(\beta, \varphi)$ in equation (8) determines the current profile within the current sheet, for which we choose

$$f(\beta,\varphi) = B_t\begin{cases} \dfrac{\beta}{\beta_o}\cos\varphi & \text{for} \quad \beta|\cos\varphi| < \beta_o, \\ sign\left(\dfrac{\pi}{2} - |\varphi|\right) & \text{for} \quad \beta|\cos\varphi| > \beta_{o0}. \end{cases} \quad (9)$$

where $\beta_o = D/R_{sM}\,\alpha_0$). The half-width of the current sheet in Z is value D at the inner edge $\alpha = \alpha_o$. Function $f(\beta, \varphi)$ can be written also as

$$f(\beta,\varphi) = \sum_{n=1}^\infty\sum_{k=1}^\infty f_{nk}J_n(\lambda_{nk}\beta)\cos n\varphi, \quad (10)$$

where λ_{nk} is a solution of the equation $J_n'(\lambda_{nk}) = 0$, as required for zero normal field at the magnetopause, and we only require the terms with n odd in our application because of the anti-symmetry of the field about the equatorial plane. The first six zeros λ_{nk} for $n = 1,3,..11$ are given in Table 1. Using the first five terms of the expansion (10) yields an accuracy of about 10^{-5} [see *Belenkaya et al.*, 2005]

[29] The coefficients f_{nk} can be calculated by taking into account the properties of the orthogonal functions as

$$f_{nk} = N_{nk}^{-1}\int_0^1\int_{-\pi}^\pi J_n(\lambda_{nk}\beta)f(\beta,\varphi)\cos n\varphi d\varphi\beta d\beta, \quad (11)$$

where the normalizing coefficient N_{nk} is given by

$$N_{nk} = \frac{\pi}{2}\left(1 - \frac{n^2}{\lambda_{nk}^2}\right) J_n^2(\lambda_{nk}).$$

The current is equal to zero outside the current sheet (for $\alpha < \alpha_0$). Inside the current sheet (i.e., for $\alpha > \alpha_o$) the current can be calculated from Maxwell's equation $\boldsymbol{j}$ = curl $\boldsymbol{B}_2/\mu_o$:

$$j_\alpha = 0 \tag{12a}$$

$$j_\beta = -\frac{B_t \sin\varphi}{\mu_o R_{sM} \alpha \beta_o} \tag{12b}$$

$$j_\varphi = -\frac{B_t \cos\varphi}{\mu_o R_{sM} \beta_o \alpha \left(\alpha^2 + \beta^2\right)}. \tag{12c}$$

The current is identically zero outside the current sheet, i.e., for $|z| > (\alpha/\alpha_o)D$ or, equivalently, $\beta\,|\cos\varphi| > \beta_o$, and for all $\alpha < \alpha_o$.

[30] The total magnetic flux in each tail lobe of the distant tail is a constant for $\alpha \to \infty$ since there is no normal component at the magnetopause and $B_z \to 0$ on the tail centre plane. This value is

$$F_\infty = B_t R_{sM}^2 \left\{ \varphi_o + \frac{1}{3}\left[2 - (2 + \beta_o)\sqrt{1 - \beta_o^2}\right]\right\}, \tag{13}$$

where $\varphi_o = \cos^{-1}\beta_o$. This equation can be used to determine B_t in equation (8) if the tail magnetic flux and the current sheet width are specified.

[31] Combining $\boldsymbol{B}_1$ and $\boldsymbol{B}_2$ to find the total tail field (see *Belenkaya et al.* [2005] for details), we finally have for $\alpha < \alpha_o$

$$B_\alpha = -\frac{B_t}{\sqrt{\alpha^2 + \beta^2}} \sum_{n=1}^{\infty}\sum_{k=1}^{\infty} f_{nk}\lambda_{nk} K_n(\lambda_{nk}\alpha_0) J_n(\lambda_{nk}\beta) I_n'(\lambda_{nk} a) \cdot \cos n\varphi \tag{14a}$$

$$B_\beta = -\frac{B_t}{\sqrt{\alpha^2 + \beta^2}} \sum_{n=1}^{\infty}\sum_{k=1}^{\infty} f_{nk}\lambda_{nk} K_n(\lambda_{nk}\alpha_0) J_n'(\lambda_{nk}\beta) I_n(\lambda_{nk} a) \cdot \cos n\varphi \tag{14b}$$

and

$$B_\varphi = \frac{B_t}{\alpha\beta} \sum_{n=1}^{\infty}\sum_{k=1}^{\infty} f_{nk} n K_n(\lambda_{nk}\alpha_0) J_n(\lambda_{nk}\beta) I_n(\lambda_{nk} a) \sin n\varphi, \tag{14c}$$

while for $\alpha > \alpha_o$ we have

$$B_\alpha = -\frac{B_t}{\sqrt{\alpha^2 + \beta^2}} \cdot \left(f(\beta,\varphi) + \sum_{n=1}^{\infty}\sum_{k=1}^{\infty} f_{nk}\lambda_{nk} I_n(\lambda_{nk}\alpha_0) J_n(\lambda_{nk}\beta) K_n'(\lambda_{nk} a) \cos n\varphi \right) \tag{15a}$$

$$B_\beta = -\frac{B_t}{\sqrt{\alpha^2 + \beta^2}} \sum_{n=1}^{\infty}\sum_{k=1}^{\infty} f_{nk}\lambda_{nk} I_n(\lambda_{nk}\alpha_0) J_n'(\lambda_{nk}\beta) K_n(\lambda_{nk} a) \cdot \cos n\varphi \tag{15b}$$

and

$$B_\varphi = -\frac{B_t}{\alpha\beta} \sum_{n=1}^{\infty}\sum_{k=1}^{\infty} f_{nk} n I_n(\lambda_{nk}\alpha_0) J_n(\lambda_{nk}\beta) K_n(\lambda_{nk} a) \sin n\varphi. \tag{15c}$$

Formulas (14) and (15) determine the tail current magnetic field everywhere inside the Hermean magnetosphere. These formulas have been derived from continuity of all three components of the magnetic field vector on the surface $\alpha = \alpha_o$. We used the expansion of $sign(\frac{\pi}{2} - |\varphi|)$ on Fourier harmonic components and the equality $x(I_n(x)K_{n+1}(x) + I_{n+1}(x)K_n(x)) = 1$. Numerical coefficients f_{nk} have been calculated by numerical integration of equation (11). We have taken the terms in the sums in equations (14) and (15) from $n = 1$ to 11 (n odd only), and from $k = 1$ to 6. To check the received accuracy the ratio $B_\beta/|B|$ at the magnetopause has been calculated and it is smaller than 10^{-3} everywhere [see also *Belenkaya et al.*, 2005].

3.4. Model Calculations for MI

[32] In sections 3.2 and 3.3 we derived, in the framework of the Paraboloidal model, the algebra for calculation of the magnetic field at an arbitrary point of the Hermean magnetosphere. At the beginning of section 3.1 we described the eight input model parameters which should be fixed before such calculations are performed (Ψ is taken to be zero). Following *Bergan and Engle* [1981], we also allow for a dipole offset from origin as a possible feature of the intrinsic planet's magnetic field. The dipole offset, Δz_d and Δy_d, in the terminator plane (x = 0) represent two additional parameters. In the following paragraph we outline the method by which these parameters are determined using the Mariner 10 data.

[33] Because of the scarcity of available data, the first step is to initialize all model parameters from simple physical estimations. After that we calculate the rms deviation between the model results and Mariner 10 data (see equation (17)). The best fit values are determined not by changing each parameter separately, but by simultaneously changing the sets of the three similar parameters (B_{M0}, Δz_d, Δy_d), (Bt, R_{sM}, R_2), (B_t, z_0, b_x), and penetrated IMF vector (b_x, b_y, b_z). The first three model parameters which fix the Hermean dipole must be the same for all of the MI and MIII flybys. The other 7 model parameters may differ to reflect the different states of the magnetosphere during the two flybys. Repetition of this procedure several times for each number of three model parameters yielded three sets of the model parameters, i.e., describing separately the inbound and outbound MI, and for the entire MIII flyby. The goal of this study was to find the Mercury dipole magnetic moment that produced the best fit to all Mariner 10 measurements. Accordingly, the dipole moment and dipole offset param-

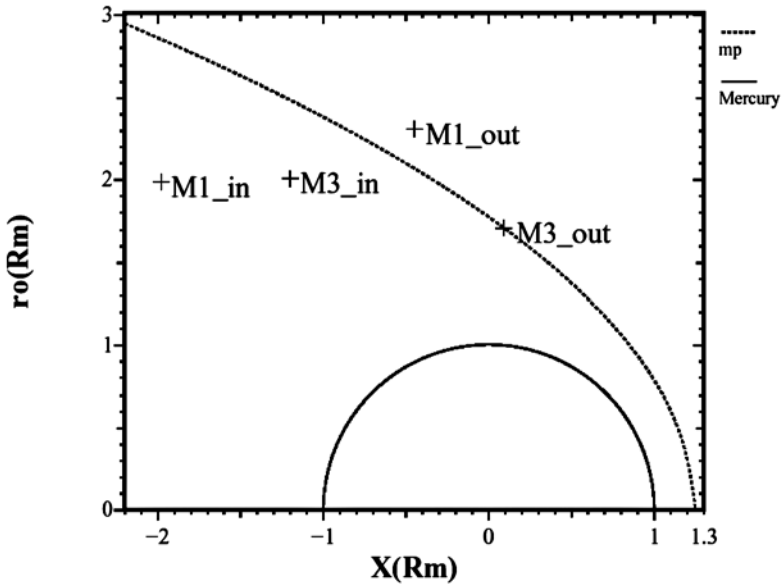

Figure 1. Paraboloid Mercury's magnetopause. Intersections of the magnetosphere boundary by Mariner 10 during MI (dashed curve) and MIII (dotted curve) flybys are marked by crosses. Coordinates of points of magnetopause crossing are taken from the study of *Slavin and Holzer* [1979a]. The aberration angle (8°) was taken into account. Along the vertical axis, the distance from the Planet-Sun line is measured in R_M.

eters were required to be the same for all three measured data sets (inbound and outbound MI and MIII).

[34] Approximating the magnetopause by a paraboloid of revolution (equation (2)), we determine the R_{sM} value. Figure 1 shows the average Mercury's paraboloid with positions of magnetospheric boundary crossings by Mariner 10 during its MI and MIII passes. From this figure it is seen that while for MI outbound and MIII the value of R_{sM} = 1.24 R_M can serve as a good approximation, for MI inbound it is impossible to draw a simple paraboloid connected with both (i.e., MI inbound and MI outbound) magnetopause crossings. *Slavin and Holzer* [1979b] emphasized that the southward IMF intervals observed during this first encounter may have had significant effects on the location of the magnetospheric boundary. For modeling the MI we can use the R_{sM} = 1.4 R_M for the solar wind pressure $P_{sw} = 6 \times 10^{-8}$ dynes/cm^2 inferred from the outbound magnetopause crossing by *Slavin and Holzer* [1979b]. Best fitting for MI data also gives the R_{sM} equal to 1.4 R_M in agreement with the estimation of *Slavin and Holzer* [1979b], which is slightly bigger than the preliminary value of R_{sM} = 1.24 R_M taken from Mariner 10 magnetopause crossings (Figure 1). The corresponding average value for R_2 is taken to be R_2 = 0.8 R_{sM} by analogy with the case of the Earth, which gives R_2 = 1.24 R_M for the MI encounter.

[35] For calculations of B_t we use the formula: $B_t = 2F_\infty/(\pi R^2{}_{sM}\ \alpha_0)$ [*Alexeev et al.*, 2003], where F_∞ is a magnetic flux in the magnetospheric tail lobe whereas $\alpha_0 = (1 + 2R_2/R_{sM})^{1/2}$. Assuming $F_\infty = \pi B_{tail} R^2{}_{tail}$, we can estimate B_t as:

$$B_t = 2F_\infty/\left(\pi R_{sM}^2 \alpha_0\right) = 2\pi B_{tail} R_{tail}^2/\left(\pi R_{sM}^2 \alpha_0\right) = 2B_{tail} R_{tail}^2/\left(R_{sM}^2 \alpha_0\right). \quad (16)$$

[36] Following *Christon* [1987], the total jump in the B_x component inside the nightside Mercury's magnetosphere for MI is 20 nT - (−90) nT = 110 nT, so the average value of B_x in the tail lobe is $B_{tail} \sim$ 110 nT/2 = 55 nT. *McKenna-Lawlor* [1997] estimated the average tail radius of Mercury's magnetopause as 2.3 R_M ± 0.3 R_M. Assuming that during the MI encounter the average values of R_{sM} and R_2 are 1.4 R_M and 1.24 R_M, respectively, and B_{tail} = 55 nT, R_{tail} = 2.3 R_M, from equation (17) we obtain B_t = 185 nT. The best fitting procedure gives smaller values of B_t equal to 165 nT and 173 nT for the inbound and outbound passes, correspondingly.

[37] Thus the flux in the tail lobe is $F_\infty = B_{tail}\pi R^2{}_{tail}$ = 55 nT $\cdot\pi\cdot 5.76 R^2{}_M$ = 994.8 nT$\cdot R^2{}_M$. If this flux determines the average co-latitude of the polar cap boundary, θ_{pc}, which is connected with the polar cap flux, $F_{pc} = 2B_{M0}\pi R^2{}_M \sin^2\theta_{pc}$, where B_{M0} is the dipole field at the Mercury's equator, then from equation $F_\infty = F_{pc}$ we obtain $B_{M0}\cdot\sin^2\theta_{pc}$ = 994.8 nT$\cdot R^2{}_M/2\pi R^2{}_M$ = 158.4 nT. As it will be demonstrated below by our fitting procedure, calculations in the Paraboloidal model with B_{M0} appropriate for both the MI and MIII flybys give $B_{M0} = -192$ nT. Thus, for MI passage, θ_{pc} = 65.3° according to the tail lobe flux estimation.

[38] Mercury's magnetic dipole moment is $\mu_M = B_{M0} R^3{}_M = 3.5 \times 10^{18}$ T cm^3 = 3.5×10^{22} G cm^3. *Slavin and Holzer* [1979b] noted that if the uneroded value of R_{sM} = 2.1 R_M for $P_{sw} = 6.0 \times 10^{-8}$ dynes/cm^2 is used, then a value of $\mu_M = 6 \pm 2 \times 10^{22}$ G cm^3 will be received. At a first step μ_M can be estimated as 240 nT$R^3{}_M$. As a result of our fitting procedure (see details below), if we require a constant dipolar field for both flybys, this initial value is ~20% higher than the final best fit Hermean dipole moment 192 nT$R^3{}_M$ (see below).

Table 2. Best Fitting Model Parameters for Both Mariner 10 Flybys With Shifted Dipole[a]

	B_{M0} (nT)	Δz_d (R_M)	Δy_d (R_M)	B_t (nT)	R_{sM} (R_M)	R_2 (R_M)	z_0 (R_M)	b_x (nT)	b_y (nT)	b_z (nT)	$\sigma_{1,2}$ (nT)	σ_3 (nT)
MI in	192	0.18	0.01	165	1.21	1.25	0.095	27	−2	20	13.76	13.08
MI out	192	0.18	0.01	173	1.33	1.35	0.32	−33	−12	21		
MIII	192	0.18	0.01	95	1.56	1.25	−0.65	24	−3	22.0	12.26	

[a]We show three sets of the best fit model parameters for the inbound and outbound passes of MI and the total MIII flyby. The order of the fitting model parameters corresponds to the number of the table's column. The equatorial dipole field (B_{M0}) is shown in the 2nd column. This dipole field gives a minimum of rms σ_3 which is placed in the last column. The total rms, σ_3, is the deviation between data and model for both flybys and for all three sets of the model parameters listed in the table. Dipole offsets (Δy_d and Δz_d) are shown in the 3rd and 4th columns. The tail field strength at the inner edge of the tail current (B_t) is shown in the 5th column. Subsolar distance (R_{sM}) is placed in the 6th column followed, in the 7th column, by the distance to the inner edge of the tail current (R_2). The tail current sheet displacement in the north-south direction relative the equatorial plane (z_0) is shown in the 8th column. Columns 9, 10, and 11 show the penetrated IMF components. Column 12 presents the best fit rms values σ_1 and σ_2 for the MI and MIII flybys, correspondingly.

[39] To fit the model parameters we calculate the rms which was determined by formula:

$$\sigma = \sqrt{\frac{\sum_{i=1}^{N} \Delta B_i^2}{N}}, \tag{17}$$

where $\Delta B_i^2 = (B_{x_obs} - B_{x_mod})^2 + (B_{y_obs} - B_{y_mod})^2 + (B_{z_obs}$ $(B_{z_obs} - B_{z_mod})^2$. Here N is a number of points in which observed (a_{obs}) and calculated (a_{mod}) values of some quantity, a, are taken. It should be noted that the formula for rms given above differs from that one which was used by *Bergan and Engle* [1981] and *Engle* [1997] for determination of σ. Unlike Engle, who used an average deviation for each component of the magnetic field vector, we use here the module of the vector which is a difference between the measured magnetic field and model magnetic field vectors. Moreover, Engle used only the first 90 data points of the MI flyby, where large disturbances were absent.

[40] At each fitting step we calculated three values determined by formula (17): σ_i, where i = 1, 2, 3. σ_1 is the rms for both inbound and outbound MI passes. For MI flyby a number of points in which we calculated the square of the difference vector between model field and measured field, was N_1 = 180. We have used data with time step 6 sec and the total duration of MI was ~18 minutes. σ_2 is the rms for MIII pass, N_2 = 157, the total duration of MIII was ~16 minutes. σ_3 is the rms for both MI and MIII flybys, $N_3 = N_1 + N_2$ = 337. Our goal is to find the set of model parameters which minimize the total rms (σ_3) for both MI and MIII flybys, the other two rms $\sigma_{1,2}$ are used to check the fitting procedure. These rms also serve as indicators of the best fit value of the model parameters which have been chosen separately for the inbound and outbound MI and MIII flybys.

[41] Finally, we will determine three sets of the model parameters, which are described at the beginning of section 3.1. These sets correspond to the inbound MI, outbound MI and MIII flyby, respectively. These sets of data have been chosen, because we propose that contrary to the dipole parameters, the IMF and solar wind conditions can change near the MI closest approach to Mercury and they can be different for the MI and MIII flybys. The dipole magnetic moment and dipole offset were taken constant for MI and MIII flybys. In Table 2 we present three sets of parameters which minimize σ_1 and σ_2. We show in Table 2 the dipole offset in the dawn −dusk direction, the best fit value of this offset is very small (about 20 km). The minimal rms are 13.6 nT for MI and 12.26 nT for MIII. These values correspond to 15% and 3% from maximum measured magnetic field for MI and MIII passes. The total rms for all existing data points is 13.08 nT. To determine the role of the dipole offset we repeat the fitting procedure, but for the centered dipole. As expected, it gives the bigger B_{M0} = 285 nT value, because offset of the centered dipole along Z axis makes a smaller minimal distance between dipole and the Mariner 10 orbit periapsis. The minimum rms values also increase in two times up to 15.3 nT, 30.3 nT and 23.5 nT for MI_{in}, MI_{out}, and for MI+MIII, correspondingly. Other four best fit parameters which are connected with magnetic field strength also increase about 1.5 times similar to dipole moments increasing. Three dimension model parameters change slightly (up to 20%). It means that they can be determined independently from each other. Thus we found that the dipole moment determined from the Mariner 10 data is 192 nT R_M^3 with the offset dipole along the Z axis Δz_d = 0.179 R_M, and along the Y axis Δy_d = 0.0083 R_M. As shown in Figure 2, the fit to the MI flyby is excellent despite within the substorm current wedge near midnight and field-aligned currents [see *Slavin et al.*, 1997]

[42] The best fit to the MI observations is found when a large "penetration" of the IMF into the magnetosphere is assumed. Upstream of the bow shock, before the Mariner 10 passage through the magnetosphere, Bx IMF was about 20 nT. However, the measured values of Bx = +20 nT in the upper tail lobe and −90 nT in the lower tail lobe [e.g., *Christon*, 1987] can be reconciled if a ΔBx ~ −30 nT is added to the tail magnetic field. Indeed, an IMF Bx component of this magnitude was measured following the outbound crossing of the magnetopause. If we assume that this field had completely penetrated into the Mercury's magnetosphere, i.e., k_{IMF} ~ 1, then the observed asymmetry in Bx in the northern and southern tail lobes can be explained. From these sets of parameters it follows, in particular, that the best fitting is achieved, if a large IMF Bx value had penetrated into the Mercury's magnetosphere with k_{IMF} ~ 1 [see also *Sarantos et al.*, 2001].

[43] To obtain the best fitting of the MI and MIII observations using the unified magnetic dipole moment we calculate σ_3, the total rms between data and model for both flybys and for all three sets of the model parameters which are listed in Table 2. The order of the fitting model parameters corresponds to the number of their Table 2 column. At first, we determine B_{M0} which gives a minimum

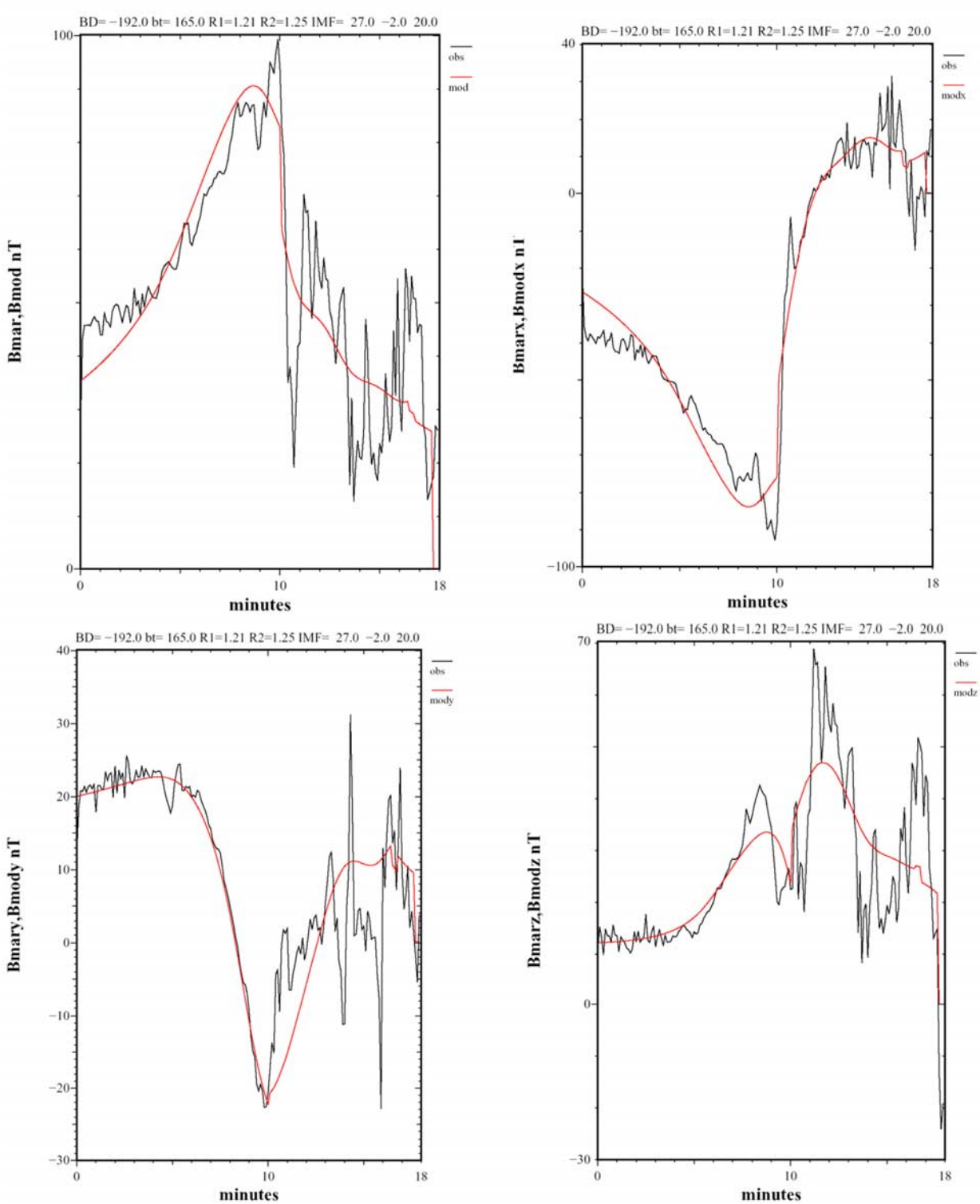

Figure 2. Unified dipole moment. Best fitting for dipole shifted up to Δz_d = 0.18 R_M above the equatorial plane. (a) Module of the observed (black curve) and calculated (red curve) magnetic field during the MI encounter. Selected parameters are $B_{M0} = -192$ nT and $\Delta z_d = 0.18\ R_M$; $B_t = 165$ nT, $R_{sM} = 1.21\ R_M$, $R_2 = 1.245\ R_M$, $z_0 = 0.095\ R_M$, $b_x = 27$ nT, $b_y = -2$ nT, and $b_z = 20$ nT; $B_{M0} = -192$ nT and $\Delta z_d = 0.18\ R_M$; and $B_t = 173$ nT, $R_{sM} = 1.33\ R_M$, $R_2 = 1.35\ R_M$, $z_0 = 0.31\ R_M$, $b_x = -33$ nT, $b_y = -12$ nT, and $b_z = 21$ nT for the inbound and outbound portions of the MI trajectory, respectively. rms $\sigma_1 = 13.76$ nT. (b) X component of the observed (black curve) and calculated (red curve) magnetic field. (c) Y component of the observed (black curve) and calculated (red curve) magnetic field. (d) Z component of the observed (black curve) and calculated (red curve) magnetic field. Tics on the horizontal axis mark the minutes from Mariner 10's first magnetopause crossing during MI flyby (20 h 36 min 50 s on 29 March 1974).

of σ_3 and after finding of this value, we go to the dipole offset Δr_d and find the next minimum of σ_3. We return to B_{M0} after finding Δr_d, because the dipole moment and dipole offset correlate with each other. When the best-fit B_{M0} and Δr_d are fixed, we go to the next parameter B_t and change it to reach a new minimum of σ_3, and etc. To check that we find the model parameters set which give the minimum of σ_3, we return to start of the best fit procedure and repeat it with initial parameter set equal results of the previous run. We repeat these runs till rms does not change after two successive runs. We obtain the best fit parameters conserved after checking run and these values are listed in Table 2. For the unified dipole moment $B_{M0} = -192$ nT, and dipole offset with the components: $\Delta z_d = 0.18\ R_M$ and $\Delta y_d = 0.01\ R_M$ the following parameter sets are selected (first and second lines of Table 2):

$$B_t = 165\text{nT}, R_{sM} = 1.21R_M, R_2 = 1.25R_M,$$
$$z_0 = 0.095R_M, b_x = 27\text{nT}, b_y = -2\text{nT}, b_z = 20\text{nT}, \quad (18)$$

$$B_t = 173\text{nT}, R_{sM} = 1.33R_M, R_2 = 1.35R_M,$$
$$z_0 = 0.31R_M, b_x = -33\text{nT}, b_y = -12\text{nT}, b_z = 21\text{nT} \quad (19)$$

for the inbound and outbound portions of the MI trajectory, respectively, with corresponding values of $\theta_{pc} = 48°$ and 56.4°. These best-fit values are about 25% smaller than our initial estimation of the polar cap radii. For this flyby and chosen parameters, the rms $\sigma_1 = 13.76$ nT. Figure 2 presents the model simulation of the MI magnetic field measured data (module of the total magnetic field, and its X, Y, and Z-components, respectively) for the unified value of the Mercury's dipole moment with the chosen offset.

3.5. Model Calculations for MIII

[44] During the third flyby the Mercury magnetosphere appeared relatively stable. The closest approach was at 22:39:23 UT. At this time the spacecraft entered a region of very low electron intensities, presumably the extensions of the lobes of the magnetotail with open field lines connected to the solar wind [see *Wurz and Blomberg*, 2001]. The IMF was northward during the entire MIII flyby [*Ness et al.*, 1976]. The mean inferred stand-off distance was 1.9 R_M [*Slavin and Holzer*, 1979b]. As it was previously noted, a paraboloid with $R_{sM} = 1.24\ R_M$ gives a good preliminary approximation for the magnetopause during MIII (see Figure 1), but the best fit procedure gives $R_{sM} = 1.56\ R_M$. To minimize the rms value for MIII, the best fitting procedure was obtained for the value of Mercury's dipole magnetic field and dipole offset determined from fitting simultaneously both MI and MIII flybys. The obtained parameters are $B_{M0} = -192$ nT and the dipole offset with $\Delta y_d = 0.0083R_M$, $\Delta z_d = 0.179R_M$. The other model parameters, which give the minimum of σ_3, are:

$$B_t = 95\text{nT}, R_{sM} = 1.56R_M, R_2 = 1.25R_M,$$
$$z_0 = -0.65R_M, b_x = 24\text{nT}, b_y = -3\text{nT}, b_z = 22\text{nT} \quad (20)$$

[45] The calculated polar cap angle radius is $\theta_{pc} = 44.2°$ for this flyby. The average rms σ_2 is 12.3 nT or about 3% from the maximum measured field. Figures 2 and 3 present comparison of observations with calculations using these model parameters. The time step on the horizontal axis is 1 min. Figure 4 shows the comparison of the discrepancy of the observed magnetic field and contributions to the magnetospheric field of the magnetopause and tail currents. The main contribution to the model field gives the dipole field (not drawn in Figure 4) which strongly increased as the spacecraft approached Mercury. However, in the outer magnetosphere the tail and magnetopause current field can be essential. If the magnetospheric field is ignored, then the deviation between the model and observation magnetic fields increases significantly.

3.6. Summary of Unified Model Results for MI and MIII

[46] In Table 2 we show three sets of the model parameters for the inbound and outbound passes of MI and the total MIII flyby. The dipole tilt is assumed to be zero in all calculations ($\Psi = 0$). The second column contains the Hermean dipole equatorial field unified for all data. The dipole offset 0.0083 R_M in the dawn-dusk direction was received, and displacement of the dipole up to 0.18 R_M along Z axis decreased the rms If we change these values (to increase or decrease B_{M0} and/or Δz_d), the rms deviation, σ_3, between the model magnetic field vector and magnetometer data, will increase. In this sense, we find the best-fit dipole moment and dipole offset values. In the third column of Table 2, the tail field strength, B_t, is shown. For MI flyby both B_t values have been chosen in such a way that the average σ for the total MI flyby be minimal. For MIII flyby this parameter is about two times smaller than for MI. This could be a result of the magnetosphere expansion and/or of the lesser level of the magnetospheric activity during the MIII flyby comparable to the MI one. The distance to the inner edge of the tail current sheet, R_2, and the tail current sheet displacement relative to the equatorial plane, z_0, demonstrate similar behavior. Values of the model parameters presented in Table 2, give the minimum σ, shown in the last tenth column. Three variables in the 7th, 8th, and 9th columns show the IMF components, which were chosen from two criteria: (1) the IMF components must be close to the Mariner 10 data outside the magnetosphere, and (2) the σ value calculated with them should be smallest. The σ values shown in the last right column present an essential part of the average measured field. These values indicate that the model could be improved by including additional modifications such as the dipole tilt.

[47] Note that we cannot determine the best fit of the k_{IMF} value, because we have no simultaneous measurements of $\boldsymbol{B}_{IMF}$ and of the magnetospheric magnetic field. However, we can estimate the most probable value of the k_{IMF} by comparison of the best-fit values of the penetrated IMF, listed in Table 2, with the average magnetic field measured outside the magnetosphere.. This estimation demonstrates that sometimes k_{IMF} can be close to 1.

[48] Our fitting procedure demonstrates that the accuracy of the Mercury dipole moment from Mariner 10 data is about 20%. Improved accuracy of the dipole offset is expected after the MESSENGER orbital phase measure-

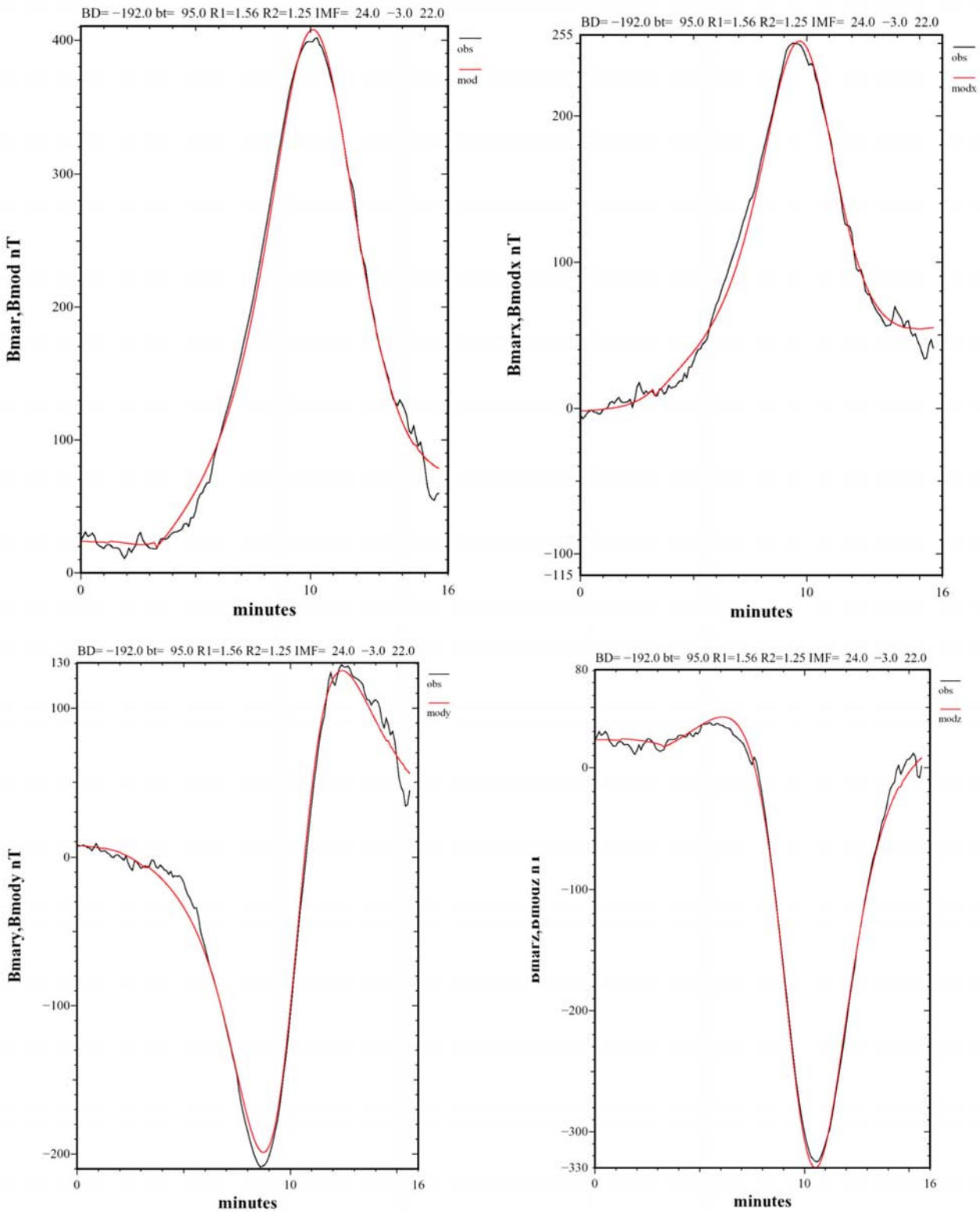

Figure 3. Best fitting for the unified dipole shifted up to $\Delta z_d = 0.18\ R_M$ along the Z axis. (a) Module of the observed (black curve) and calculated (red curve) magnetic field during the MIII encounter. Found best fit model parameters are $B_{M0} = -192$ nT and $\Delta z_d = 0.18\ R_M$ and $B_t = 95$ nT, $R_{sM} = 1.56\ R_M$, $R_2 = 1.25\ R_M$, $z_0 = -0.65\ R_M$, $b_x = 24$ nT, $b_y = -3$ nT, and $b_z = 22$ nT for the MIII flyby. rms $\sigma_2 = 12.26$ nT. (b) X component of the observed (black curve) and calculated (red curve) magnetic field. (c) Y component of the observed (black curve) and calculated (red curve) magnetic field. (d) Z component of the observed (black curve) and calculated (red curve) magnetic field. Tics on horizontal axis mark the minutes from the first Mariner 10 magnetopause crossing during MIII flyby (22 h 29 min 30 min on 16 March 1975).

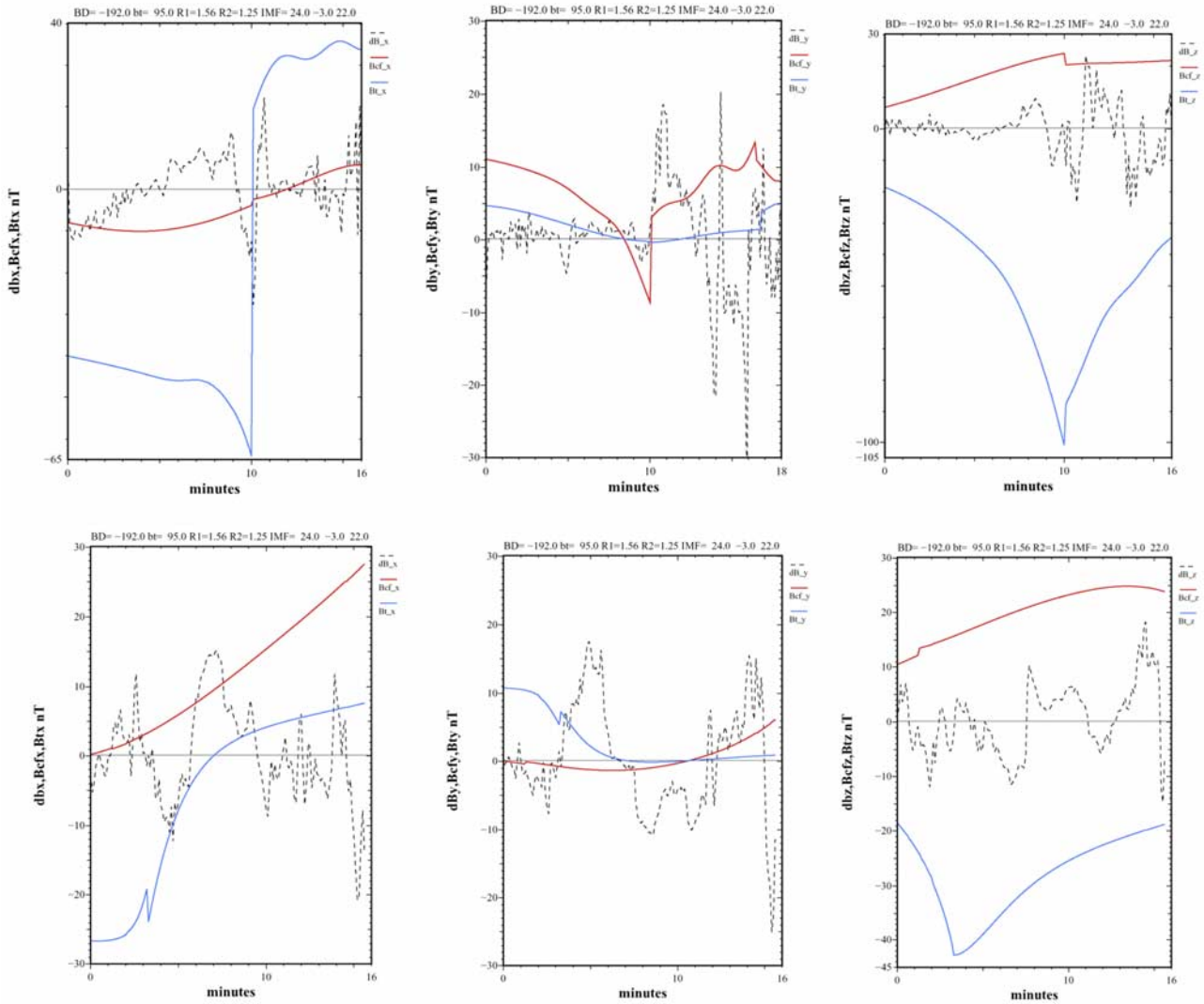

Figure 4. Relative contributions of the magnetospheric global current systems to the total magnetic field. The top row shows for the MI flyby the three components of the magnetopause currents (red curve), the tail currents (blue curves), and the difference between the Mariner 10-measured magnetic field components and the model forecast dB_x, y, z = (Bobs − Bmod) _x, y, z (dashed curves). The bottom row demonstrates the same magnetopause and tail current contributions to the model field along MIII orbit. The dashed curves illustrate the difference between the observed magnetic field and the magnetic field vectors calculated by the model.

ments become available [*Anderson et al.*, 2007]. MESSENGER orbits will cover all longitudinal sectors over a wide interval of the Mercury's northern latitudes.

4. Comparison With Other Mercury Magnetospheric Magnetic Field Models

[49] Table 3 presents a summary of our results and those by models previously applied to the M10 data. We mark by asterisk the number which was not mentioned in the original paper (by *Luhmann et al.* [1998]), but is calculated by us. In the first column in Table 3 there are five published magnetospheric models. LRT 98 indicates the model by *Luhmann et al.* [1998], and S&B 06 corresponds to *Scuffham and Balogh* [2006]. The next five columns give (from left to right) for each model: (2) M_{M} (the Mercury magnetic moment); (3) R_{sM} (the magnetopause subsolar distance); (4) R_t (the distance to the inner edge of the tail current); (5) θ_{pc} is the polar cap radius determined by us from the figure with noon-midnight field lines; and (6) k_{IMF} is the ratio of the penetrated into the magnetosphere interplanetary magnetic field portion to the origin IMF. All distances in Table 3 have been determined from the noon-midnight field line drawings in the corresponding papers.

[50] Our Mercury magnetosphere model offers several distinct advantages over previous models. For example, the models of *Engle* [1997] and *Scuffham and Balogh* [2006] used their own representations for the magnetopause and tail currents similar to our approach. However, our parameterization of the tail current system has only two parameters: (1) the distance to the inner edge of the current sheet, and (2) the tail lobe magnetic flux. Furthermore, as already

Table 3. Comparison of Different Mercury's Magnetospheric Models[a]

Model	M_M (nT R_m^3)	R_{sM} (R_M)	R_t (R_M)	θ_{pc} (deg)	k_{IMF}
Engle 97	154–182	1.2	1.5	30	0
LRT 98	~180*	1.4	1.2	47	1.0
Lukyanov et al. 01	300	1.4	1.5	50	0
Korth et al. 04	300	2.2	1.5	36	0
S&B 06	228	1.2	~2.8	35	0.5
This study (MI)	192	1.27	1.3	52	1.0
This study (MIII)	192	1.56	1.25	44	0.4
This study (extreme)	192	1.0	1.0	60	1.0

[a]The first column lists five published magnetospheric models. LRT 98 indicates the model by *Luhmann et al.* [1998], and S&B 06 corresponds to that of *Scuffham and Balogh* [2006]. The next five columns give (from left to right) for each model: (2) M_m (the Mercury magnetic moment); (3) R_{sM} (the magnetopause subsolar distance); (4) R_t (the distance to the inner edge of the tail current); (5) θ_{pc} is the polar cap radius determined by us from the figure with noon-midnight field lines; (6) k_{IMF} is the ratio of the penetrated into the magnetosphere interplanetary magnetic field portion to the origin IMF.

demonstrated, both of these parameters can be directly and independently determined from the magnetometer measurements taken during the two Mariner 10 magnetospheric encounters. By comparison, the models of Engle and Scuffham and Balogh employ more than ten parameters which have been determined to describe the Earth's tail current sheet density space distribution. This strongly increases the number of arbitrary parameters which may influence the final results. In our case we use paraboloid harmonic expansions, a universal treatment for the Neumann problem, and we only parameterize the total current amplitude.

[51] The most widely used approach to estimate the magnetic field due to magnetospheric current systems during the Mariner 10 encounters is to scale the Tsyganenko terrestrial magnetosphere models [*Tsyganenko*, 2002, and references therein] to Mercury using simple spatial scaling [see *Luhmann et al.*, 1998; *Korth et al.*, 2004]. However, there are several disadvantages and limitations to this approach at Mercury:

[52] 1. The Tsyganenko models are based upon an extensive database of measurements taken at Earth that may not be representative of Mercury's magnetosphere, especially with respect to the relative contributions of the different magnetospheric current systems. For example, as demonstrated by *Engle* [1997], and by our results, the magnetopause and tail currents have different scaling factors. Furthermore, *Fairfield and Jones* [1996] showed that the tail lobe field strength depends on the solar wind dynamic pressure, p_{sw}, as $p_{sw}^{1/4}$ whereas the dayside magnetic field inside of the magnetopause goes as $p_{sw}^{1/2}$. Accordingly, the ratio of the magnetopause to tail current density will increase by a factor of $(1/r)^{1/2} \sim 1.4$ in going from Earth at 1 AU to Mercury's perihelion at 0.3 AU.

[53] 2. The two Mariner 10 encounters show that the intensity of Mercury's magnetospheric current systems and their relative contributions to the total magnetic field can be highly variable depending upon the upstream solar wind and IMF conditions. The response of Mercury's magnetosphere to IMF orientation and reconnection appears to be more rapid and intense than what is observed at the Earth. For this reason the paraboloidal model's inclusion of "penetration" by all 3 components of the IMF into Mercury's magnetosphere with a specified coefficient may be an especially important advantage of our model over the scaled Tsyganenko models, which do not incorporate the dominant radial component. Different approaches used different values for two scaling factors (for space and for magnetic field). It is clearly demonstrated in Table 3 that the magnetic field factor, k_m, changes from 2 (LRT 98) to 5.1 [*Lukyanov et al.*, 2001], while the space scaling factor, k_s, changes from 4.6 [*Korth et al.*, 2004] to 8 [*Lukyanov et al.*, 2001].

[54] Of course, once large magnetic field databases are collected at Mercury by the MESSENGER and BepiColombo missions it will be possible to determine the many semi-empirical parameters required by Tsyganenko-type models and to produce Mercury-specific magnetospheric current system models. Presently only a limited number of measurements of Mercury's magnetospheric magnetic field is available from the two Mariner 10 flybys. For all of the reasons listed earlier our procedure is concentrated not on a dimension scaling of the Earth-specific magnetosphere models, but rather on a simple, robust model containing the minimum number of free parameters to provide an accurate representation of the magnetic field with the additional requirement that these parameters all be determined from the available Mercury measurements. The Paraboloidal model meets both of these requirements and it has been successfully tested for the magnetospheres of Earth, Jupiter and Saturn.

5. Mercury's Magnetosphere Under Extreme Conditions

[55] As a further application of the Paraboloidal model, we examine the response of Mercury's magnetosphere to extreme solar outbursts. The solar wind conditions that exert the maximum stress upon magnetospheres are: (1) high-dynamic pressure which applies stress normal to the magnetopause, compressing the planetary magnetic field and reducing the magnetospheric volume; and (2) strong interplanetary magnetic fields with significant components antiparallel to the subsolar magnetic field at the magnetopause, resulting in dayside reconnection that splices together the IMF and magnetospheric flux tubes. This latter interaction reduces the volume of the dayside magnetosphere while increasing the volume of the nightside magnetosphere and the diameter of the magnetic tail. Further, dayside reconnection exerts a tangential stress on the magnetosphere that results in a high rate of transfer of solar wind energy into the magnetosphere and increases the effective "penetration" of the IMF into the magnetosphere.

[56] The most extreme instances of high solar dynamic pressure and intense north-south interplanetary magnetic fields are generally found in association with interplanetary coronal mass ejections (ICMEs). It is for this reason that ICMEs are among the most "geoeffective" conditions found in the solar wind and they produce the largest magnetospheric storms at the Earth. Figure 5 displays an example of an interplanetary (IP) shock driven by a ICME identified by *Liu et al.* [2005] in the Helios 1 observations taken near Mercury's orbit, i.e., at 0.34 AU from the Sun, on 20 June 1981. Solar wind dynamic pressure and the interplanetary electric field potential drop across a trans-

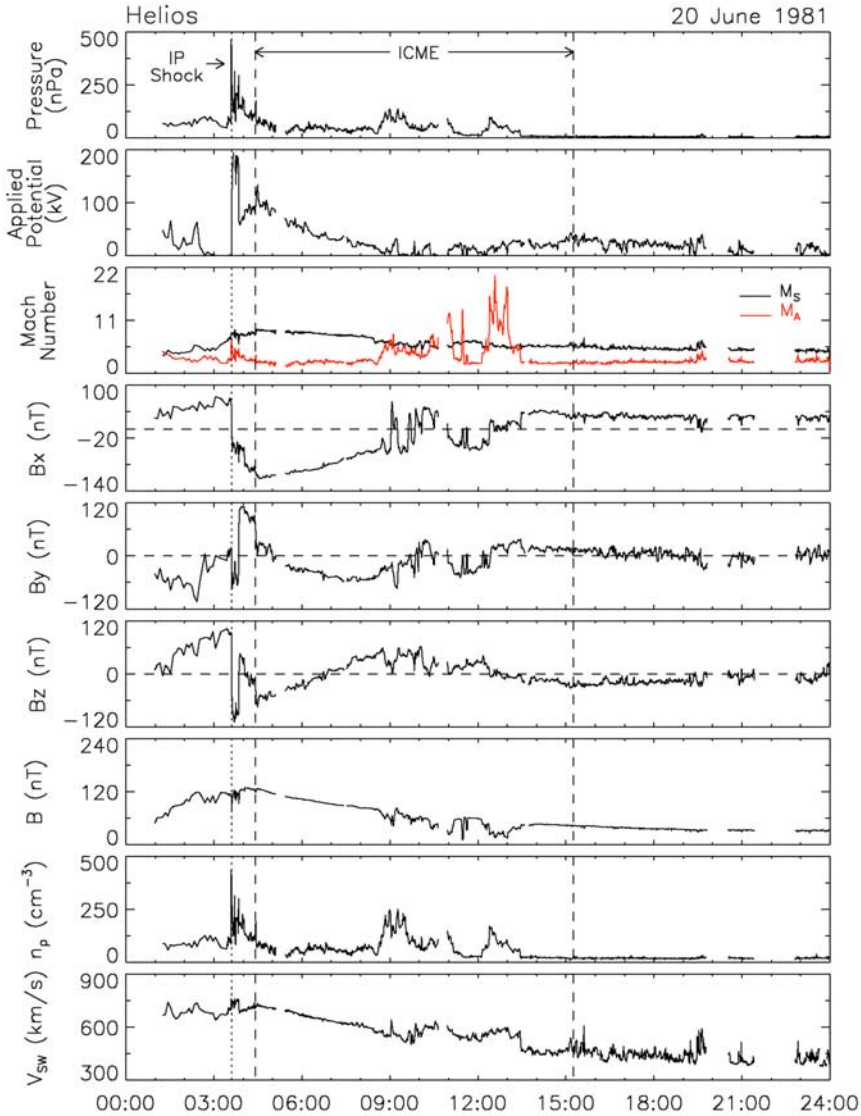

Figure 5. Solar wind and IMF measurements from the Helios 1 spacecraft during an ICME observed at 0.34 AU are presented. The event was identified from the list presented by *Liu et al.* [2005]. From top to bottom, the panels display solar wind dynamic, or ram pressure; applied potential drop $(-V_{sw} \times B_{yz}) \bullet L$ across a magnetospheric scale length $L = 1\ R_M$; Alfvenic (red) and sonic (black) Mach numbers; the three components of the IMF and the total field intensity; and, finally, in the lower two panels, the solar wind density and speed. Note that, during ICME events, the Mercury's magnetosphere can experience extreme conditions, with the solar wind dynamic pressure reaching 500 nPa applied electric potential dropping across the magnetosphere of 200 kV and Alfvenic Mach number values below 2.

verse length scale comparable to Mercury's magnetosphere, i.e., $\sim$1.5 R_M, spike at nearly 500 nPa and 200 kV, respectively, during and just after the arrival of the ICME-driven interplanetary shock around $\sim$ 3:30 UT. The ICME itself is composed of relatively cool coronal plasma. The intense north-south magnetic fields are due to the embedded large magnetic flux rope. The ICME is observed over a $\sim$ 12 hr interval beginning about an hour after the IP shock passes Helios. The strongest north–south magnetic fields, at times exceeding ±100 nT are associated with the IP shock, the IMF draped and compressed about the ICME, and the flux rope core of the ICME itself.

[57] After the ICME passage (i.e., past 15:00 on 20 June 1981) the solar wind pressure was about 1.3 nPa. The average solar wind pressure at 0.31–0.35 AU according to the Helios data is 20 nPa. The subsolar point pressure balance gives the magnetopause subsolar distance $R_{sM} = 1.27\ R_M$ for the average conditions and the dipole moment 192 nT R_M^3, in agreement with our best fit data for the MI orbit. Below we study the two cases with extreme magnetosphere conditions. One of them is for a low solar wind pressure 1.3 nPa and $R_{sM} \sim p_{sw}^{-1/6} = 2\ R_M$, and the other is for a high solar wind pressure when the magnetopause is placed near the planet $R_{sM} = 1.1\ R_M$ (pressure more than 84 nPa).

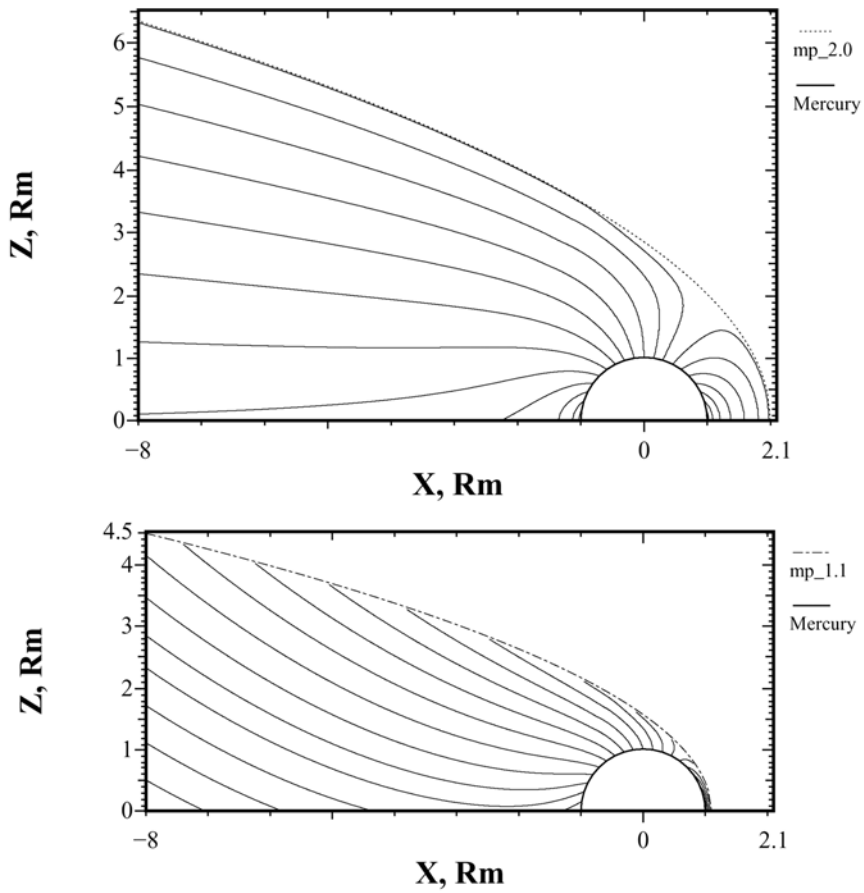

Figure 6. The two extreme states of the Mercury magnetosphere are shown. In the bottom, the maximum compression of the magnetosphere by the CME-like solar wind is shown, whereas in the top, the Hermean magnetosphere is seen to substantially expand (~x2) under low-solar-wind-pressure conditions (~1 nPa). The magnetospheric model parameters in the top are $R_{sM} = 2\ R_M$ (the magnetopause subsolar distance); $\theta_{pc} = 37.5°$ is the polar cap radius determined by the tail lobe magnetic flux; and $k_{IMF} = 0$ is the ratio of the penetrated into the magnetosphere interplanetary magnetic field portion to the origin IMF. For the bottom, the respective parameters are: $R_{sM} = 1.1\ R_M$, $\theta_{pc} = 47°$, and $k_{IMF} = 0.375$. The B_z IMF for the bottom is equal to −40 nT.

[58] The top of Figure 6 shows the magnetic configuration of Mercury's magnetosphere in the noon – midnight plane according to the Paraboloidal model for extremely weak solar wind conditions possible around the Hermean aphelion. The model parameters for this weakly driven or low external stress level were selected as follows: $R_{sM} = 2\ R_M$ (the magnetopause subsolar distance); $\theta_{pc} = 35°$ is the polar cap radius determined by the tail lobe magnetic flux; and $k_{IMF} = 0$ is the ratio of the penetrated into the magnetosphere interplanetary magnetic field portion to the origin IMF (i.e., northward IMF). As shown, the Paraboloidal model with these input parameters produces a relatively large Hermean magnetosphere with zero magnetic field normal to the magnetopause and B_z northward in the equatorial regions of the nightside magnetosphere.

[59] The bottom of Figure 6, on the other hand, depicts the possible configuration of Mercury's magnetosphere in response to extreme solar wind conditions such as those associated with ICMEs. In the absence of induction effects (which are likely for IP shock events; see *Glassmeier* [1997]), our unified model of Mercury's magnetosphere predicts that the solar wind pressure will depress the magnetopause to the surface of the planet for pressures greater than 84 nPa. For this reason, Figure 6 presents the magnetic configuration of Mercury's magnetosphere for a near-maximal compression with $R_{sM} = 1.1\ R_M$. The magnetic field at the subsolar point is 470 nT. For such "extreme" conditions at Mercury, the magnetospheric magnetic field scaling factor $k_m = B_m/B_E$ is equal to 8.9, the space scaling factor k_s is equal to 10, the distance to the inner edge of the tail current sheet, $R_t = 1.0\ R_M$, and the polar cup radius will be $\theta_{pc} = 60°$. As shown in the bottom of Figure 6, under these conditions the Paraboloidal model produces a dayside magnetosphere that doesn't extend significantly beyond the surface of Mercury and a relatively large magnetic field component normal to the magnetopause. The strong "penetration" of the IMF into the magnetosphere for these strong southward IMF conditions alters the topology of the equatorial nightside magnetosphere with the B_z magnetic field becoming southward beyond $X \sim -2.5\ R_M$. This is the same relative distance down the tail where the near-Earth

neutral line forms in the Earth's magnetosphere [*Slavin*, 2004].

[60] In this manner, the Paraboloidal model can be used to explore how Mercury's magnetosphere is expected to vary in its spatial extent and magnetic field intensity because of the extreme variations in solar wind and IMF found in the inner heliosphere, especially when the Sun is most active around Solar Maximum and ICMEs are common. However, large external stresses and inputs of solar wind energy to this small magnetosphere are also expected during the high-speed streams that are common during the declining phase of the Solar Cycle.

6. Conclusions

[61] A new model of Mercury's global magnetospheric current systems has been developed based upon the Paraboloidal Model which has been successfully applied previously to the Earth [*Alexeev*, 1978, 1986; *Alexeev et al.*, 2003], Jupiter [*Alexeev and Belenkaya*, 2005; *Belenkaya*, 2004], and Saturn [*Belenkaya et al.*, 2006, 2007; *Alexeev et al.*, 2006]. The magnetospheric current model includes the magnetopause current that confines the planet's magnetic field to the magnetosphere and the tail current system consisting of the cross-tail current sheet and the closure currents at the magnetopause.

[62] Using this model we have re-examined the Mariner 10 observations taking into account the IMF penetration into the magnetosphere and the global magnetospheric currents at the time of each encounter. Under the assumption that the solar wind interaction with Mercury is terrestrial in character, it was shown that the contribution of the external current systems to the total magnetic field in the vicinity of Mercury is significant even at the planet's surface. Determination of a rotation axis-aligned magnetic dipole moment value, 192 nT R_M^3, that is consistent with both of the Mariner 10's close encounters is one of achievements of the present work. We also found strong evidence for a dipole offset by up to 0.18 R_M in the northward direction, but more accurate calculations of the dipole position will require new measurements from the MESSENGER mission.

[63] Comparison of the model calculations with data obtained during the Mariner 10 MI and MIII flybys shows the important role which the IMF plays in the Mercury's magnetosphere. Analysis of the magnetic field measurements indicates that the coefficient of the IMF penetration into the Hermean magnetosphere is much larger than at the Earth and may approach unity when the upstream IMF is southward. This result supports earlier suggestions that magnetic reconnection between the planetary magnetic field and the IMF may be much more efficient at Mercury as compared to the Earth because of the lower Alfven Mach numbers found in the inner heliosphere [*Slavin and Holzer*, 1979a].

[64] NASA's MESSENGER mission will be inserted into an orbit around Mercury in 2011 [*Solomon et al.*, 2001]. The ESA - JAXA BepiColombo mission, now in development [*Schulz and Benkhoffa*, 2006], will arrive Mercury in 2019 and will consist of both a low-altitude planetary orbiter and a higher apoapsis magnetospheric orbiter. However, while we await these new measurements from Mercury orbit, significant improvements in our understanding of Mercury's intrinsic magnetic field and magnetospheric currents are expected to result from the measurements to be collected during three MESSENGER flybys (January and October 2008; September 2009).

[65] **Acknowledgments.** Work at the Institute of Nuclear Physics, Moscow State University, was supported by the RFBR Grant 07-05-00529. MS was supported by the NASA Postdoctoral Program (NPP).

[66] Wolfgang Baumjohann thanks the reviewers for their assistance in evaluating this paper.

References

Abramowitz, M., and I. A. Stegun (1972), *Handbook of Mathematical Functions*, 8th ed., chap. 9, p. 177, Dover, Mineola, New York.

Alexeev, I. I. (1978), Regular magnetic field in the Earth's magnetosphere (in Russian), *Gemagnetizm Aeronom.*, *18*, 656–665. (*Geomagn. Aeron.*, Engl. Transl., *18*, 447–452.)

Alexeev, I. I. (1986), The penetration of interplanetary magnetic and electric fields into the magnetosphere, *J. Geomagn. Geoelectr.*, *38*, 1199–1221.

Alexeev, I. I., and E. S. Belenkaya (2005), Modelling of the Jovian Magnetosphere, *Ann. Geophys.*, *23*, 809–826.

Alexeev, I. I., and V. P. Shabansky (1972), A model of a magnetic field in the geomagnetosphere, *Planet. Space Sci.*, *20*, 117–133.

Alexeev, I. I., E. S. Belenkaya, S. Yu. Bobrovnikov, and V. V. Kalegaev (2003), Modelling of the electromagnetic field in the interplanetary space and in the Earth's magnetosphere, *Space Sci. Rev.*, *107*, 7–26.

Alexeev, I. I., V. V. Kalegaev, E. S. Belenkaya, S. Y. Bobrovnikov, E. J. Bunce, S. W. H. Cowley, and J. D. Nichols (2006), A global magnetic model of Saturn's magnetosphere, and a comparison with Cassini SOI data, *Geophys. Res. Lett.*, *33*, L08101, doi:10.1029/2006GL025896.

Anderson, B. J., M. H. Acuña, D. A. Lohr, J. Scheifele, A. Raval, H. Korth, and J. A. Slavin (2007), The MESSENGER magnetic fields experiment, *Space Sci. Rev.*, *131*, 417–540, doi:10.1007/s11214-007-9246-7.

Anderson, B. J., M. H. Acuña, H. Korth, M. E. Purucker, C. L. Johnson, J. A. Slavin, S. C. Solomon, and R. L. McNutt Jr. (2008), The structure of Mercury's magnetic field from MESSENGER's first flyby, *Science*, *321*, 82–86.

Beard, D. B. (1979), The magnetotail magnetic field, *J. Geophys. Res.*, *84*, 2118–2122.

Belenkaya, E. S. (2004), The Jovian magnetospheric magnetic and electric fields: Effects of the interplanetary magnetic field, *Planet. Space Sci.*, *52*, 499–511.

Belenkaya, E. S., S. Y. Bobrovnikov, I. I. Alexeev, V. V. Kalegaev, and S. W. H. Cowley (2005), A model of Jupiter's magnetospheric magnetic field with variable magnetopause flaring, *Planet. Space Sci.*, *53*, 863–872.

Belenkaya, E. S., S. W. H. Cowley, and I. I. Alexeev (2006), Saturn's aurora in the January 2004 events, *Ann. Geophys.*, *24*, 1649–1663.

Belenkaya, E. S., I. I. Alexeev, M. S. Blokhina, S. W. H. Cowley, S. V. Badman, V. V. Kalegaev, and M. S. Grigoryan (2007), IMF dependence of the open-closed field line boundary in Saturn's ionosphere, and its relation to the UV auroral oval observed by the Hubble Space Telescope, *Ann. Geophys.*, *25*, 1215–1226.

Bergan, S., and I. M. Engle (1981), Mercury's magnetosphere and magnetotail revised, *J. Geophys. Res.*, *86*, 1617–1620.

Blomberg, L. G. (1997), Mercury's magnetosphere, exosphere and surface: Low-frequency field and wave measurements as a diagnostic tool, *Planet. Space Sci.*, *45*(1), 143–148.

Boardsen, S. A., and J. A. Slavin (2007), Search for pick-up ion generated Na^+ cyclotron waves at Mercury, *Geophys. Res. Lett.*, *34*, L22106, doi:10.1029/2007GL031504.

Cheng, A. F., R. E. Johnson, S. M. Krimigis, and L. Z. Lanzerotti (1987), Magnetosphere, exosphere, and surface of Mercury, *Icarus*, *71*, 430–440.

Christon, S. P. (1987), A comparison of the Mercury and Earth magnetospheres: Electron measurements and substorm time scales, *Icarus*, *71*, 448–471.

Connerney, J. E. P., and N. F. Ness (1988), Mercury's magnetic field and interior, in *Mercury*, edited by F. Vilas, C. R. Chapman, and M. S. Matthews, pp. 494–513, Univ. of Arizona Press, Tucson, Ariz.

Engle, I. M. (1997), Mercury's magnetosphere: Another look, *Planet. Space Sci.*, *45*(1), 127–132.

Fairfield, D. H., and J. Jones (1996), Variability of the tail lobe field strength, *J. Geophys. Res.*, *101*(A4), 7785–7792.

Giampieri, G., and A. Balogh (2001), Modelling of magnetic field measurements at Mercury, *Planet. Space Sci.*, *49*, 1637–1642.

Glassmeier, K. H. (1997), The Hermean magnetosphere and its I-M coupling, *Planet. Space Sci.*, *45*, 119–125.

Glassmeier, K. H., J. Grosser, U. Auster, D. Constantinescu, Y. Narita, and S. Stellmach (2007), Electromagnetic induction effects and dynamo action in the Hermean system, *Space Sci. Rev.*, *132*(2-4), 511–527.
Gradshteyn, I. S., and I. M. Ryzhik (1971), Tables of integral, sums, expansions and products (in Russian), p. 689, points 6.525 (1), Nauka, Moscow, Russ. (See also "Tables of Integral Transforms," vol. II, McGraw-Hill Book Company, Inc., New York, p. 63, formula (8), 1954).
Grard, R. (1997), Photoemission on the surface of Mercury and related electric phenomena, *Planet. Space Sci.*, *45*(1), 67–72.
Greene, J. M., and R. L. Miller (1994), The field of a screened magnetic dipole, *Planet. Space Sci.*, *42*, 895–902.
Ip, W.-H. (1986), The sodium exosphere and magnetosphere of Mercury, *Geophys. Res. Lett.*, *13*, 423–426.
Ip, W.-H., and A. Kopp (2002), MHD simulation of the solar wind interaction with Mercury, *J. Geophys. Res.*, *107*(11), 1348, doi:10.1029/2001JA009171.
Jackson, D. J., and D. B. Beard (1977), The magnetic field of Mercury, *J. Geophys. Res.*, *82*, 2828–2836.
Hunten, D. M., T. M. Morgan, and D. M. Shemansky (1988), The Mercury atmosphere, in *Mercury*, edited by F. Vilas, C. Chapman, and M. Matthews, pp. 562–612, Univ. of Arizona Press, Tucson, Ariz.
Kabin, K., T. I. Gombosi, D. L. DeZeeuw, and K. G. Powell (2000), Interaction of Mercury with the solar wind, *Icarus*, *143*, 397–406.
Kabin, K., M. H. Heimpel, R. Rankin, J. M. Aurnou, N. Gómez-Pérez, J. Paral, T. I. Gombosi, T. H. Zurbuchen, P. L. Koehn, and D. L. DeZeeuw (2008), Global MHD modeling of Mercury's magnetosphere with applications to the MESSENGER mission and dynamo theory, *Icarus*, *195*(1), 1–15.
Kallio, E., and P. Janhunen (2003a), Solar wind and magnetospheric ion impact on Mercury's surface, *Geophys. Res. Lett.*, *30*(17), 1877, doi:10.1029/2003GL017842.
Kallio, E., and J. P. Janhunen (2003b), Modeling the solar wind interaction with Mercury by a quasi-neutral hybrid model, *Ann. Geophys.*, *21*(11), 2133–2145.
Killen, R. M., A. E. Potter, P. Reiff, M. Sarantos, B. V. Jackson, P. Hick, and B. Giles (2001), Evidence for space weather at Mercury, *J. Geophys. Res.*, *106*, 20,509–20,525.
Korth, H., B. J. Andersona, M. H. Acuna, J. A. Slavin, N. A. Tsyganenko, S. C. Solomon, and R. L. McNutt Jr. (2004), Determination of the properties of Mercury's magnetic field by the MESSENGER mission, *Planet. Space Sci.*, *52*, 733–746.
Lammer, H., and S. J. Bauer (1997), Mercury's exosphere: Origin of surface sputtering and implications, *Planet. Space Sci.*, *45*, 73–79.
Liu, Y., J. D. Richardson, and J. W. Belcher (2005), A statistical study of the properties of interplanetary coronal mass ejections from 0.3 to 5.4 AU, *Planet. Space Sci.*, *53*, 3–17.
Luhmann, J. G., C. T. Russell, and N. A. Tsyganenko (1998), Disturbances in Mercury's magnetosphere: Are the Mariner 10 "substorms" simply driven, *J. Geophys. Res.*, *103*(A5), 9113–9119.
Lukyanov, A. V., S. Barabash, R. Lundin, and P. C. Brandt (2001), Energetic neutral atom imaging of Mercury's magnetosphere. 2: Distribution of energetic charged particles in a compact magnetosphere, *Planet. Space Sci.*, *49*, 1677–1684.
McKenna-Lawlor, S. M. P. (1997), Characteristic boundaries of the Hermean magnetosphere and energetic particles close to the planet, *Planet. Space Sci.*, *45*(1), 167–180.
Ness, N. F. (1979), The magnetosphere of Mercury, in *Solar System Plasma Physics*, vol. II, edited by C. Kennel, L. J. Lanzerotti, and E. Parker, pp. 183–206, North-Holland, Amsterdam, Netherlands.
Ness, N. F., K. W. Behannon, R. P. Lepping, Y. C. Whang, and K. H. Schatten (1974), Magnetic field observations of near Mercury: Preliminary results from Mariner 10, *Science*, *185*, 151–160.
Ness, N. F., K. W. Behannon, R. P. Lepping, and Y. C. Whang (1975), The magnetic field of Mercury, *J. Geophys. Res.*, *80*(19), 2708–2716.
Ness, N. F., K. W. Behannon, R. P. Lepping, and Y. C. Whang (1976), Observations of Mercury's magnetic field, *Icarus*, *28*, 479–488.
Ogilvie, K. W., J. D. Scudder, V. M. Vasyliunas, R. E. Hartle, and G. L. Siscoe (1977), Observations at the planet Mercury by the plasma electron instrument: Mariner 10, *J. Geophys. Res.*, *82*, 1807–1824.
Potter, A. E., T. H. Morgan, and R. M. Killen (1999), Rapid changes in the sodium exosphere of Mercury, *Planet. Space Sci.*, *47*, 1441–1448.
Russell, C. T. (1977), On the relative locations of the bow shocks of the terrestrial planets, *Geophys. Res. Lett.*, *4*, 387–390.
Russell, C. T. (1989), ULF waves in the Mercury magnetosphere, *Geophys. Res. Lett.*, *16*, 1253–1256.
Sarantos, M., P. H. Reiff, T. W. Hill, R. M. Killen, and A. L. Urquhart (2001), A Bx-interconnected magnetosphere model for Mercury, *Planet. Space Sci.*, *49*, 1629–1635.
Sarantos, M., R. M. Killen, and J. Kim (2007), Predicting the long-term solar wind ion sputtering source at Mercury, *Planet. Space Sci.*, *55*(11), 1584–1595.
Schulz, R., and J. Benkhoffa (2006), BepiColombo: Payload and mission updates, *Adv. Space Res.*, *38*(4), 572–577.
Scuffham, J., and A. Balogh (2006), A new model of Mercury's magnetospheric magnetic field, *Adv. Space Res.*, *38*, 616–626.
Shue, J.-H., et al. (1998), Magnetopause location under extreme solar wind conditions, *J. Geophys. Res.*, *103*, 17,691–17,700.
Siscoe, G. L., and L. Christopher (1975), Variations in the solar wind standoff distance at Mercury, *Geophys. Res. Lett.*, *2*, 158–160.
Siscoe, G. L., N. F. Ness, and C. M. Yeates (1975), Substorms on Mercury?, *J. Geophys. Res.*, *80*, 4359–4363.
Slavin, J. A. (2004), Mercury's magnetosphere, *Adv. Space Res.*, *33*, 1859–1874.
Slavin, J. A., and R. E. Holzer (1979a), On the determination of the Hermean magnetic moment: A critical review, *Phys. Earth Planet. Inter.*, *20*, 231–236.
Slavin, J. A., and R. E. Holzer (1979b), The effect of erosion on the solar wind stand-off distance at Mercury, *J. Geophys. Res.*, *84*, 2076–2082.
Slavin, J. A., and R. E. Holzer (1981), Solar wind flow about the terrestrial planets. 1: Modeling bow shock position and shape, *J. Geophys. Res.*, *86*, 11,401–11,418.
Slavin, J. A., J. C. J. Owen, J. E. P. Connerney, and S. P. Christon (1997), Mariner 10 observations of field-aligned currents at Mercury, *Planet. Space Sci.*, *45*(1), 133–141.
Slavin, J. A., et al. (2007), MESSENGER: Exploring Mercury's magnetosphere, *Space Sci. Rev.*, *131*, 133–160.
Slavin, J. A., et al. (2008), Mercury's magnetosphere after MESSENGER's first flyby, *Science*, *321*, 85–89.
Solomon, S. C., et al. (2001), The MESSENGER mission to Mercury: Scientific objectives and implementation, *Planet. Space Sci.*, *49*(14-15), 1445–1465.
Stern, D. (1985), Parabolic harmonics in magnetospheric modeling: The main dipole and the ring current, *J. Geophys. Res.*, *90*, 10,851–10,863.
Toffoletto, F. R., and T. W. Hill (1993), A non-singular model of the open magnetosphere, *J. Geophys. Res.*, *98*, 1339–1344.
Travnicek, P., P. Hellinger, and D. Schriver (2007), Structure of Mercury's for different pressure of the solar wind: Three dimensional hybrid simulations, *Geophys. Res. Lett.*, *34*, L05104, doi:10.1029/2006GL028518.
Tsyganenko, N. A. (1989), A magnetospheric magnetic field model with a warped tail current sheet, *Planet. Space Sci.*, *37*, 5–17.
Tsyganenko, N. A. (1995), Modeling the Earth's magnetospheric magnetic field confined within a realistic magnetopause, *J. Geophys. Res.*, *100*, 5599–5612.
Tsyganenko, N. A. (2002), A model of the near magnetosphere with a dawn-dusk asymmetry. Mathematical structure, *J. Geophys. Res.*, *107*(A8), 1179, doi:10.1029/2001JA000219.
Whang, Y. C. (1977), Magnetospheric magnetic field of Mercury, *J. Geophys. Res.*, *82*, 1024–1030.
Wurz, P., and L. Blomberg (2001), Particle populations in Mercury's magnetosphere, *Planet. Space Sci.*, *49*, 1643–1653.
Zurbuchen, T. H., J. M. Raines, G. Gloeckler, S. M. Krimigis, J. A. Slavin, P. L. Koehn, R. M. Killen, A. L. Sprague, R. L. McNutt Jr., and S. C. Solomon (2008), MESSENGER observation of the composition of Mercury's ionized exosphere and plasma environment, *Science*, *321*, 90–92.

I. I. Alexeev, E. S. Belenkaya, and S. Yu. Bobrovnikov, Institute of Nuclear Physics, Lomonosov Moscow State University, P.O. Box 119991, Leninskie Gory, Moscow, Russia.
M. Sarantos and J. A. Slavin, Heliophysics Science Division, NASA GSFC, Code 670, Greenbelt, MD 20771, USA. (james.a.slavin@nasa.gov)